Evaluation of Environmental Stresses on GNSS-Monuments

Master Thesis

written at the
Institute of Geodesy and Geophysics at Vienna University of Technology

and the
Department of Earth and Space Sciences at Chalmers University of Technology

supervised by
Dr.techn. Sten Bergstrand - SP Technical Research Institute of Sweden
Dipl.-Ing Dr.techn. Rüdiger Haas - Chalmers University of Technology
Dipl.-Ing. Dr.techn. Andreas Wieser - Vienna University of Technology

written by
Wolfgang Matthias Lehner
Untere Hauptstraße 180
7100 Neusiedl am See
Matr.Nr.: 0325719

Vienna, 08/22/2011

_____

Abstract

The aim of this thesis is to analyze four different constructions of GNSS-antenna monuments with respect to deformations due to solar radiation, temperature variations and wind. It was commissioned by Lantmäteriet, the Swedish mapping, cadastral and land registration authority and realized in cooperation between Vienna University of Technology and Chalmers University of Technology. In the first part of the project a simulation with a finite element modelling program was calculated. The values gained from the simulations reached a maximum of 1.4 mm due to wind, 1.2 mm due to solar radiation and 0.8 mm due to thermal expansion. In the second part outdoor measurements were carried out at Onsala Space Observatory where a sample of each monument type was installed. With modern Leica TS30 total stations and precision retro-reflection prisms displacements of up to 4 mm were measured. The mast that Lantmäteriet suggested, deformed the least compared to the other three. Its maximum displacement in height and position was less than one millimeter.

Zusammenfassung

Ziel dieser Arbeit ist, vier verschiedene Konstruktionen von GNSS-Antennenmonumenten auf Deformation aufgrund von Solarstrahlung, Wind und Temperaturvariationen zu untersuchen. Dieses Projekt wurde von Lantmäteriet, dem schwedischen Bundesamt für Vermessungeswesen, in Auftrag gegeben und in Kooperation zwischen der technischen Universität Wien und der Chalmers University of Technology durchgeführt. Im ersten Abschnitt wurden die zu erwartenden Verformungen mithilfe des FEM-Simulationsprogrammes "Autodesk Robot" berechnet. Dabei ergaben sich Maximalwerte von 1.4 mm aufgrund der Windbelastung, 1.2 mm aufgrund von Solarstrahlung und 0.8 mm aufgrund von thermaler Ausdehnung. Im zweiten Abschnitt wurde jeweils ein Modell der vier Konstruktionen am Onsala Space Observatory in Schweden aufgebaut und in einem dreimonatigen Messprogramm untersucht. Für die Messungen wurden Leica TS30 Totalstationen verwendet. Die Messdaten ergaben Verschiebungen der Mastspitzen von bis zu 4 mm. Eine der vier Konstruktionen wurde von Lantmäteriet vorgeschlagen, welche auch die geringsten Deformationen von horizontal und vertikal weniger als einem Millimeter ergab.

Acknowledgements

First of all I want to thank my family for supporting me during my studies and my year abroad in Sweden.

A special thank goes to my supervisors Dr.techn. Sten Bergstrand, Dipl.-Ing. Dr.techn. Rüdiger Haas and Dipl.-Ing. Dr.techn. Andreas Wieser. They supported me with patience and gave many improvement suggestions which motivated me to increase the quality of my work.

I want to thank Magnus Herbertsson, G-G Svantesson and Jörgen Spetz from the geometry section of SP for supporting me on my work by providing measuring equipment as the ball prisms and the calibrated steel bar for calculating the base length and orientation of the total stations. I am very grateful that they controlled my adjustment calculation with a laser tracker.

Many people at Onsala Space Observatory have also been very helpful. Lars Wennerbäck, Håkan Millqvist and Christer Hermansson from the workshop built up all masts and were always available for any request of mine. Lars Petterson, Lars Ericsson, Roger Hammargren and Karl-Åke Johansson from the technical staff at Onsala Space Observatory supported me on IT-problems and electronic equipment, e.g. cables, digital multimeter, and so on.

Christer Thunell and Hans Borg from Leica Geosystems Sweden were very helpful in software and hardware questions concerning the Leica total stations.

Tobias and Marlene Neal read through and gave improvement ideas for the written part of this thesis.

I also want to thank Martin Lidberg and Bo Jonsson, who supported me at Lantmäteriet in Gävle.

Contents

Introduction

GNSS is the abbreviation for "Global Navigation Satellite System". Today, there are two operative GNSS, the American GPS and the Russian Glonass. In the near future further GNSS are expected to become operational, e.g. the European Galileo system. GNSS are used worldwide for a variety of applications connected to positioning and navigation on the Earth's surface, in the atmosphere and in space.

Lantmäteriet, the Swedish mapping, cadastral and land registration authority, uses GNSS for its SWEPOS network, the Swedish national network of permanent reference stations for GNSS. There are a large number of SWEPOS stations distributed over Sweden, and these are used for many purposes, from real-time positioning with an accuracy of meters to geodetic measurements with millimeter accuracy. The highly accurate geodetic measurements are used for geophysical research, e.g. concerning glacial isostatic adjustment (GIA) processes.

The equipment for highly accurate GNSS-measurements includes dedicated monuments that carry the GNSS-antennas that receive the satellite signals. These monuments need to be stable in order to avoid that the GNSS-measurements are influenced by any deformation of the monuments themselves, e.g. due to environmental influences such as wind, solar radiation and temperature variations. Lantmäteriet plans to complement the existing SWEPOS stations in the coming years by additional new GNSS-monuments. A new monument design is under consideration: a steel truss tower of 3.2 m height (see Figure 1.1.1). Its behavior with respect to environmental influences needs to be evaluated and compared to three alternative designs. The three alternative designs were a straight steel mast with reinforcement plates on 3 sides, a hexagonal tapered steel mast, both of similar height to the truss mast, and a shorter pyramid shaped construction of only 1.2 m height constructed by four steel rods (see Figures 1.2.1, 1.3.1 and 1.4.1).

The master thesis project consisted of two complementary parts. The first part concentrated on simulations using the finite element method (FEM). The four different monument designs were modeled with the FEM software "Autodesk Robot" and exposed theoretically to different environmental stress by thermal and wind forces. The FEM software calculated the expected deformations due to these environmental influences (see Section 2.1). The second part included high precision geodetic measurements at the Onsala Space Observatory where prototypes of the four alternative GNSS-monuments were erected. The measurement system consisted of two motorized

total stations of type Leica TS30, 6 retro-reflecting mini prisms of type Leica GMP 104, 4 retro-reflecting prisms of type Leica RFI, several temperature sensors and one pyranometer. Wind information was retrieved from the standard meteorological sensors at the observatory.

The two total stations were set up directly on stable bedrock. For this purpose, corresponding 5/8 inch screws were attached to the bedrock to allow mounting the corresponding tribraches of the total stations. Three retro-reflecting prisms were set up in a similar way directly on stable bedrock and well distributed around the baseline between the two total stations. The remaining seven retro-reflecting prisms were attached at the four steel monuments. The steel truss mast was covered by a protective plastic pipe that during future operation should prevent people from climbing on the mast. An additional advantage is that the pipe blocks solar radiation. The temperature sensors were mounted on several places, i.e. directly on the masts in both the sun and the shade, and inside and outside the protective pipe in the air.

The motorized total stations were programmed and computer controlled to perform distance and angle measurements in two faces to all prisms with a repeating cycle of ten minutes. The software that was used to program the total stations was Leica GeoMos. Additionally, temperature measured at different places, wind and solar radiation were recorded with high temporal resolution of one minute. In total, three months of monitoring observations were carried out, covering different environmental conditions.

To find the exact distance between the rotational centers and the relative orientations of both total stations an adjustment calculation using the least squared method (LS) and the least median squared method (LMS) was performed. It was possible to control these values with a laser tracker later in the project. The coordinate determination to all retro-reflecting prisms was realized by forward intersection from both total stations and by polar point calculations from each total station as well.

Maximal displacements of up to 4 mm have been measured, where daily movements on the order of a tenth of a mm were also found.

Chapter 1

Analyzed Monuments

1.1 Lantmäteriet truss mast (LM)

One construction that has been analyzed is a truss monument that Lantmäteriet suggested (see Figure 1.1.1). It is made of steel and has an equilateral triangle with 30 cm base length as horizontal section. The overall height of the mast is 3.20 m. There is an additional extension at the top of the mast which should ensure good signal receiving conditions.

There was also a protective pipe installed around the monument (see Figure 1.1.1c) which should prevent people from climbing on the mast. The change of the antennas coordinates by even a few millimeters would drastically falsify the results gained from the calculations with the measurement values of that GNSS-antenna. The protective pipe is not connected to the truss construction such that wind forces acting on the pipe are not being transmitted to the mast. In Figure 1.1.1d one can see that there were some holes in the bottom part of the pipe. By drilling the holes air circulation inside the pipe was achieved. Therefore the effect of heat accumulation was avoided. An additional advantage of the pipe is that it blocks the sun and keeps the mast in the shade. As the pipe does not reach up to the antenna, the last 30 cm of the construction give the total amount of horizontal deformations due to solar radiation.

Moreover, the analysis of the deformation behavior of the mast under different conditions was carried out. For a certain amount of time the holes in the bottom of the mast were closed with glue strips to prevent air circulation. For the third scenario no protective pipe was used.

In Figure 1.1.1b one Leica GMP 104 prism, that defined the reference point to measure all deformations, is presented. It has been fixed on a screw that was welded directly on the steel construction.

To be able to distinguish between bending and tilting of the mast, three small ball prisms were additionally mounted on the bottom part of the mast which defined a layer in each epoch that gave information about the correlation between the displacement at the top and the tilt of the mast. It turned out that the accuracy of the measurements to the ball prisms was not good enough to reach meaningful values. As shown in Section

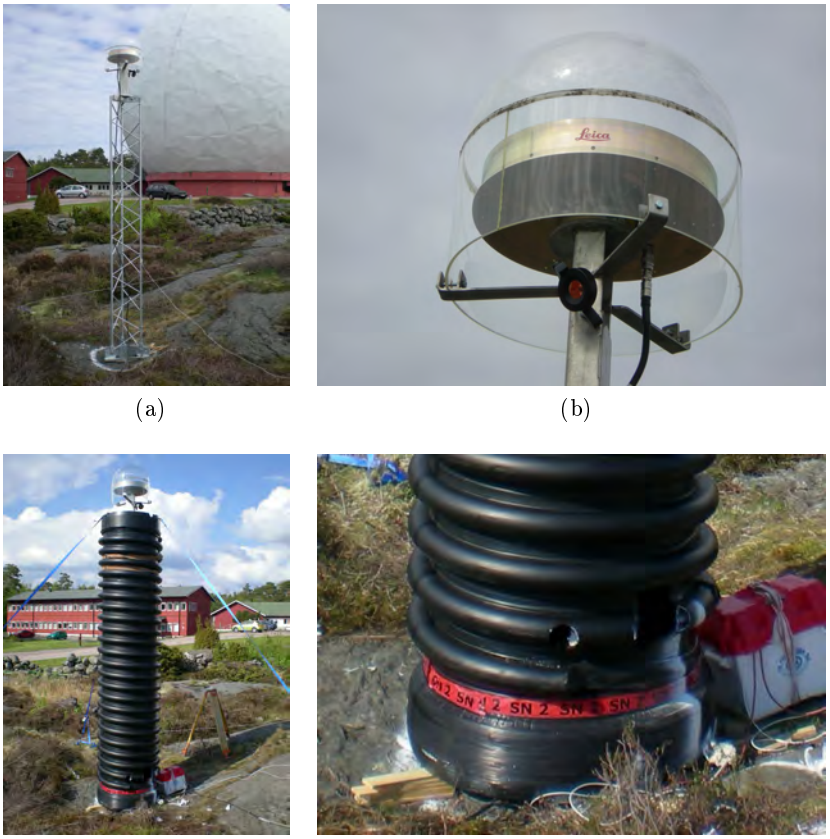

(a) (b)

(c) (d)

Figure 1.1.1: Lantmäteriet truss construction
a) Prism mounting at the top of the mast. b) Mast without protective pipe.
c) Mast with protective pipe. d) Holes for air circulation at the mast bottom.

7.1, displacements of up to 0.8 mm were measured at the LM-mast, which means that it would have been necessary to obtain the change in height of the ball prisms with an accuracy of 0.05 mm. The empirical standard deviation of the height of the prisms at the LM-mast bottom is with 0.15 mm too much for using the prisms in the calculations (see Section 5.4.2).

The installation was done with four screws that reached 10 cm into stable bedrock. After drilling the holes, a special glue was used to fix the screws in the bedrock (see Figure 1.1.2).

Figure 1.1.2: Mounting of the total station in the bedrock

1.2 Straight mast with reinforcement plates on three sides (Earlconic construction - EC)

(a) Mast construction (b) Prism mounting at the top of the mast

Figure 1.2.1: EC-mast

The second construction is a straight mast with reinforcement plates on three sides (see Figure 1.2.1). That type is already in use in the USA ([Semenchuk, 2007]) where the analyzed one, as the LM-mast, has a height of 3.20 m to set almost the same conditions for both types of a GNSS-monument. It is hollow, has a material thickness of 3 mm and a diameter of 10 cm. On the top, only the radome of a GNSS-antenna has been installed. Inside there was a bucket with some stones that had the same weight as the antenna to ensure the same wind attracting area at all masts. The reason for this is the necessity of equal conditions to be able to compare the results. Here, the prism

was again mounted on a screw that was welded directly under the antenna (see Figure 1.2.1b).

The installation has been realized, as with the LM-mast construction, with four screws that have been drilled 10 cm into stable bedrock.

1.3 Tapered hexagonal mast (SALSA)

Another construction that has been analyzed is a hexagonal steel mast that has a diameter at the bottom of 20 cm and at the top of 10 cm. This type of construction is in use for measurements with SALSA radio telescopes at Onsala Space Observatory.

The optimal solution has been found by simulating all combinations of diameters from 5 to 25 cm with an FEM-Simulation program. It is hollow, 3.20 m high and also has a metal thickness of 3 mm. As with the EC-mast, a radome was mounted with a bucket of stones to simulate an antenna which was needed to measure deformations due to wind. The monument was fixed in the stable bedrock by screws which have been drilled 10cm into stable bedrock. The prism as reference point has been mounted directly under the antenna radome. (see Figure 1.3.1b)

(a) Mast construction (b) Prism mounting at the top of the mast

Figure 1.3.1: Hexagonal mast used for SALSA radiotelescopes at Onsala Space Observatory

1.4 Shallow drilled braced monument (SDBM)

The fourth construction is built out of telescope steel rods which were arranged in the shape of a three sided pyramid with one additional rod in the center (see Figure 1.4.1a).

It is, in contrast to the other analyzed constructions, much smaller at 1.25 m in height. It is in use in the USA (see [UNAVCO, 2010]) but under different conditions. In that project, the monument was installed with screws on bedrock in contrast to the

ones that are in use already. Those are used in areas where there is no stable base and the stabilizing rods are fixed up to 7 meters into the ground.

For that construction a special ball prism (Leica RFI) was used which was fixed on the construction by using a glueing pistol directly under the pseudo antenna (see Figure 1.4.1b).

(a) Mast construction (b) Prism mounting at the top of the mast

Figure 1.4.1: SDBM-mast used in the USA

Chapter 2

FEM-Simulations

In order to see the prospective deformations during all the outdoor measurements it was necessary to simulate the measurements in an FEM-program, called "Autodesk Robot" in advance. FEM is the abbreviation for "Finite Element Method". It is a numerical technique for finding approximate solutions of partial differential equations as well as of integral equations. One scope of application is the modelling of displacements and internal forces of complex structures due to external forces. The basic principle is to separate a given structure in a finite number of elements with known characteristics. To find the displacement of one element the following integrating steps need to be calculated:

Force $\rightarrow$ Stress $\rightarrow$ Strain $\rightarrow$ Displacement

$$f \rightarrow \sigma \rightarrow \varepsilon \rightarrow u$$

By finding the force equilibrium in all nodes connecting the elements, the overall displacement and internal forces can be found.

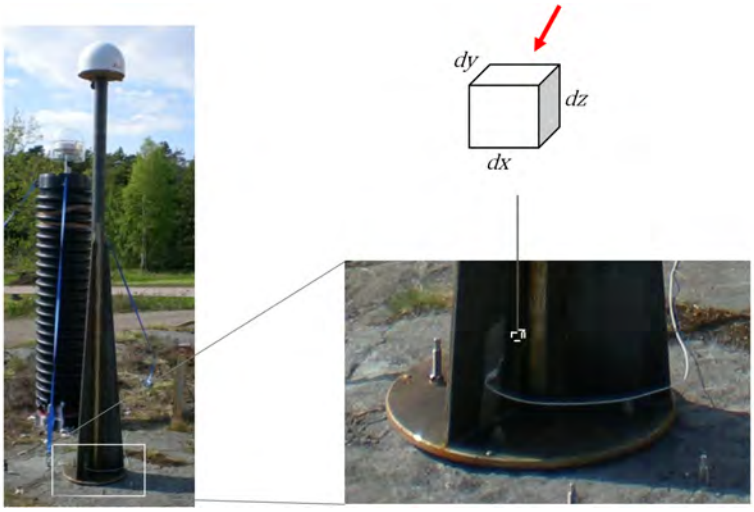

Figure 2.1: Structure seperated in finite elements

2.1 Results from FEM-simulations

For the simulations the following assumed forces have been used:

1. Metal temperature difference between sun and shade due to solar radiation: 5°C
2. Daily change in temperature of up to 20°C
3. Wind: 30 m/s

In Sections 5.1 and 5.2 it is shown, that during the entire measurement period wind speeds up to 18 m/s, daily temperature variations of up to 18° and metal temperature differences between sun and shade of up to 8°C were measured. The highest wind speed ever measured in Sweden was 40 m/s.

As the dimensions of the SALSA-mast were not given, several different realizations of this construction were simulated in Autodesk Robot.

All combinations of diameters from 10 to 25 cm at the bottom and 5 to 20 cm at the top have been analyzed. Based on the results (see Figure 2.1.1) of the simulations it was decided to choose the mast with diameters of 20 cm at the bottom and 10 cm at the top.

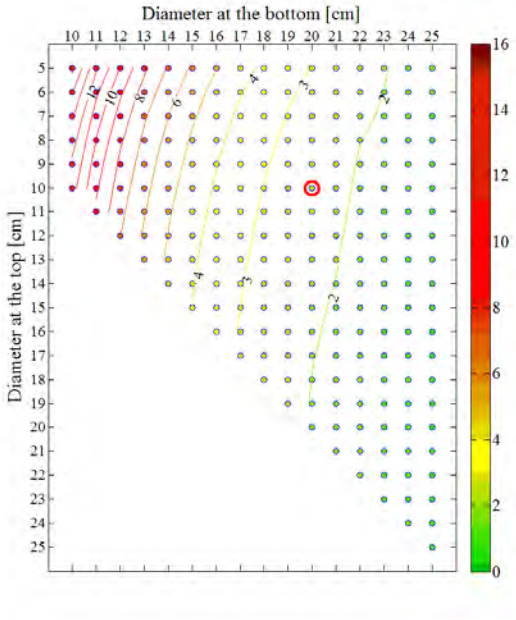

Figure 2.1.1: Deformations of different realizations of hexagonal masts

Additionally the bending effects due to solar radiation on different shapes have been analyzed. Masts with a constant bottom diameter and variable top diameters give following results:

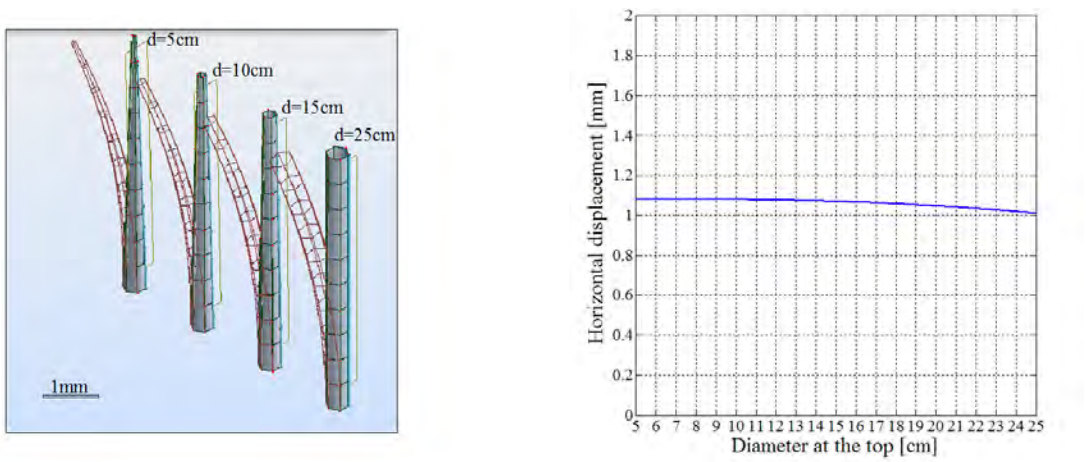

Figure 2.1.2: Deformation of hexagonal masts with a constant bottom diameter of 25 cm and variable top diameters

The deformation varies very little with at most 0.05 mm therefore a diameter of just 10 cm has been chosen. With that diameter an optimal area of support in relation to connection stability between antenna and mast, and signal quality has been found.

Straight masts with different diameters of 5, 10, 15, 20 and 25 cm give the following results:

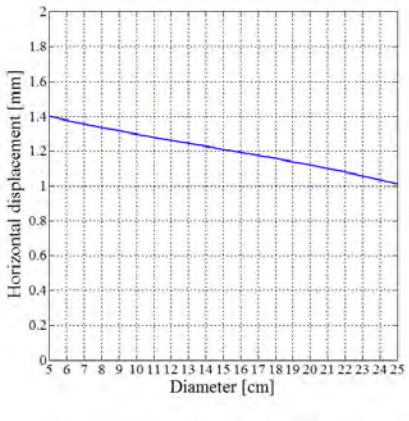

Figure 2.1.3: Deformation of straight hexagonal masts with different diameters

Figure 2.1.3 shows, as expected, that slimmer masts deform more than broader ones, as the distance between the cold and warm sides of the metal structure is shorter on slim masts than on broad ones. The differences are not much, but to ensure good mounting conditions in the ground, a relatively broad construction, with a diameter of 20 cm at the bottom, was chosen.

All deformations resulted from the simulations are summarized in Table 2.1.1

Table 2.1.1: FEM Simulations: Deformations due to wind, solar radiation and temperature

Max. deformations [mm]	**Wind (30 m/s)**	**Sun (ΔT=5 °C)**	**Temp. (ΔT=20 °C)**
LM-mast (h=3.20 m)	0.4	0.2	0.8
EC-mast (h=3.20 m)	1.4	1.0	0.8
SALSA-mast (h=3.20 m)	1.2	1.2	0.8
SDBM-mast (h=1.25 m)	<0.1	0.1	0.4

Chapter 3

Calculations

3.1 Orientation

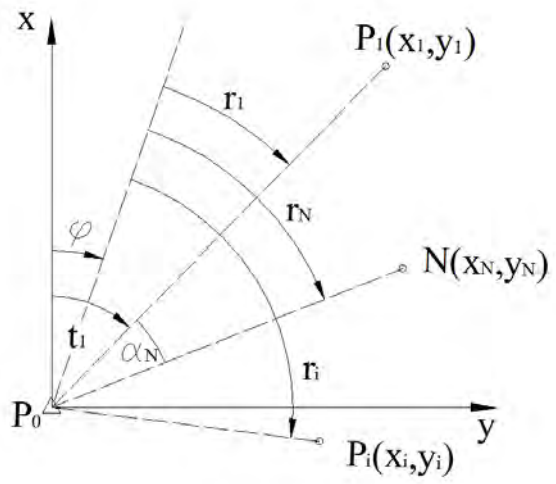

Figure 3.1.1: Principle of orientation calculation (following Kahmen, 2006)

The triangles in Figure 3.1.1 show that the point has given coordinates in contrast to points with a circle as symbol of which the coordinates are not known. In the beginning all measured directions are oriented arbitrarily. The orientation of the directions can be found by rotating the null direction in the abscissa direction of the coordinate system that is used for the calculations. That angle is also known as orientation unknown. [Kahmen, 2006]

3.1.1 Orientation with one connection point

The given data are the point coordinates of P_0 and P_1 and the measured directions r_1 and r_N from P_0 to the given point P_1 and the unknown point N. The orientated direction t_N from P_0 to N has to be calculated by

$$t_N = r_N + \varphi \tag{3.1.1}$$

Where the orientation angle is obtained from

$$\varphi = t_1 - r_1 \tag{3.1.2}$$

t_1 is calculated by

$$t_1 = \arctan \frac{\Delta y_1}{\Delta x_1} \tag{3.1.3}$$

An alternative is to use the "reduced direction" α_N (see Figure 3.1.1) which is readily obtained from the measured directions.

$$t_N = t_1 + \alpha_N \tag{3.1.4}$$

3.1.2 Orientation with multiple connection points

The given data are the coordinates of n points P_0,P_2,...,P_n and the measured directions from point P_0. Due to measurement errors the orientation unknown is ambiguous. A suitable result is the arithmetic mean if all calculated φ_i have the same standard deviation σ_{φ_i}.

$$\bar{\varphi} = \frac{1}{n} \sum_{i=1}^{n} (t_i - r_i) \tag{3.1.5}$$

The orientated direction to the new point can then be calculated by

$$t_N = r_N + \varphi \tag{3.1.6}$$

The discrepancies between the orientated directions and the grid bearings are

$$v_i = t_i - (r_i + \bar{\varphi}) \tag{3.1.7}$$

The precision of the mean orientation unknown $\bar{\varphi}$ can be described by the empirical standard deviation:

$$\sigma_{\bar{\varphi}} = \sqrt{\frac{v^T v}{n \cdot (n-1)}} \tag{3.1.8}$$

In case of large distance variations, a weighted mean for calculating the orientation unknown would result in better values.

3.2 Coordinate calculation with forward intersection

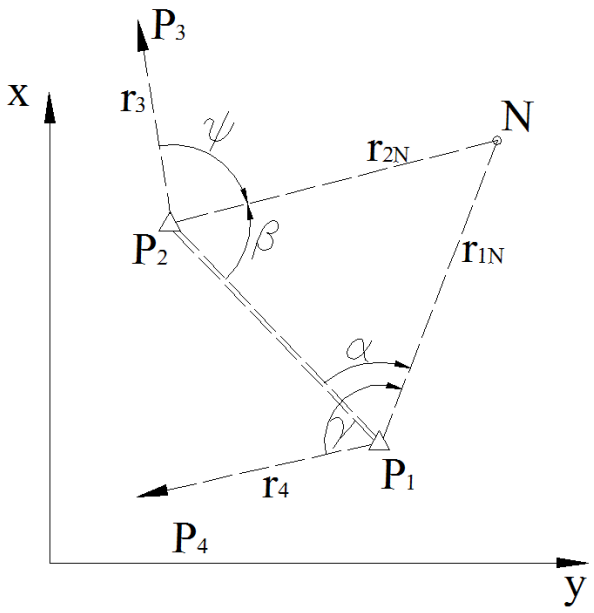

Figure 3.2.1: Principle of forward intersection (following Kahmen, 2006)

Forward intersection is a method which uses only direction measurements in order to calculate the coordinates of a new point N (see Figure 3.2.1). One calculates point coordinates by measuring directions from at least two known points (e.g. P_1, P_2 in Figure 3.2.1) to one unknown point. This method is used when high accuracy is required or the point is not accessible and reflectorless measurements are not possible. The accuracy is dependent on the geometry of the point distribution.

By measuring from a point with known coordinates indexed by i (in Figure 3.2.1 $i \in \{1, 2\}$) to one with unknown coordinates N the following equation can be found:

$$r_i = \arctan\left(\frac{y_N - y_i}{x_N - x_i}\right) - \varphi_i \tag{3.2.1}$$

r_i are the measured directions, y_N and x_N the unknown coordinates of N and y_i and x_i the known coordinates of the points from which the measurements were carried out (P_1 and P_2 in Figure 3.2.1). The orientation unknowns φ_i can be calculated as described in Section 3.1 by using measurements to points with known coordinates (P_3 and P_4 in Figure 3.2.1).

3.2.1 Calculation with linear intersection

One possibility to solve a forward intersection problem is by intersecting two lines given as:

$$y_N - y_1 = \tan(t_{1N})(x_N - x_1) \tag{3.2.2}$$

$$y_N - y_2 = \tan(t_{2N})(x_N - x_2) \tag{3.2.3}$$

where the direction parameters are given by

$$t_{1N} = t_{14} + \delta \tag{3.2.4}$$

$$t_{2N} = t_{23} + \varepsilon \tag{3.2.5}$$

After solving for the orientation parameters, the coordinates can be calculated using

$$x_N - x_1 = \frac{(y_2 - y_1) - (x_2 - x_1)\tan(t_{2N})}{\tan(t_{1N}) - \tan(t_{2N})} \tag{3.2.6}$$

$$y_N - y_1 = (x_N - x_1)\tan(t_{1N}) \tag{3.2.7}$$

To review the correctness of the coordinate calculation of the new point N, the following equations can be used

$$x_N - x_2 = \frac{(y_2 - y_1) - (x_2 - x_1)\tan(t_{2N})}{\tan(t_{1N}) - \tan(t_{2N})} \tag{3.2.8}$$

$$y_N - y_2 = (x_N - x_2)\tan(t_{2N}) \tag{3.2.9}$$

In this thesis the center of the local coordinate system was set in the rotational center of the western total station and the easting axis was defined in direction of the rotational center of the eastern total station. The equations become therefore much simpler:

$$P_1 = \begin{pmatrix} 0 \\ 0 \end{pmatrix} \tag{3.2.10}$$

$$P_2 = \begin{pmatrix} y_2 \\ 0 \end{pmatrix} \tag{3.2.11}$$

$$x_N = \frac{y_2}{\tan(t_{1N}) - \tan(t_{2N})} \tag{3.2.12}$$

$$y_N = x_N \cdot \tan(t_{1N}) \tag{3.2.13}$$

$$y_N - y_2 = x_N \cdot \tan(t_{2N}) \tag{3.2.14}$$

The y-coordinate of N calculated by using Equation 3.2.13 has to result in the same values as by using Equation 3.2.14.

3.2.2 Accuracy of forward intersection

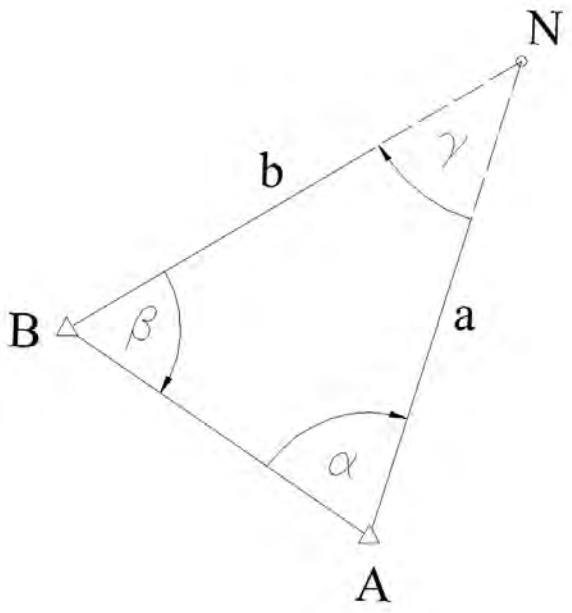

Figure 3.2.2: Accuracy of forward intersection (following Kahmen [2006])

The accuracy of the forward intersection is dependent on the accuracy of the direction measurements and the shape of the triangle P_1P_2N. The Helmert position error σ_p of N can be calculated using the standard deviation of the orientated directions σ_{r^0}, the side lengths a and b of N to $P_1$and P_2 and the included angle γ between NP_1 and NP_2:

$$\sigma_p = \frac{1}{\sin\gamma}\sqrt{a^2+b^2}\cdot\sigma_{r^0} \tag{3.2.15}$$

Equation 3.2.2 works if both orientated directions have the same standard deviation σ_{r^0} and the coordinates of the given points P_1 and P_2 are error free. σ_p becomes a minimum for $\alpha = \beta$ when the intersection angle γ is 121 gon. If γ is 0 or 200 gon the calculation becomes instable as then a division by zero would emerge.

For distances a and b between 7.5 m and 1.8 m (see Section 4.3), standard deviations of the used total stations Leica TS30 of 0.15 mgon in direction measurement (see Section 4.1.1), a Helmert Position error between 0.02 mm and 0.29 mm emerges.

3.3 Coordinate calculation with distance and direction measurements

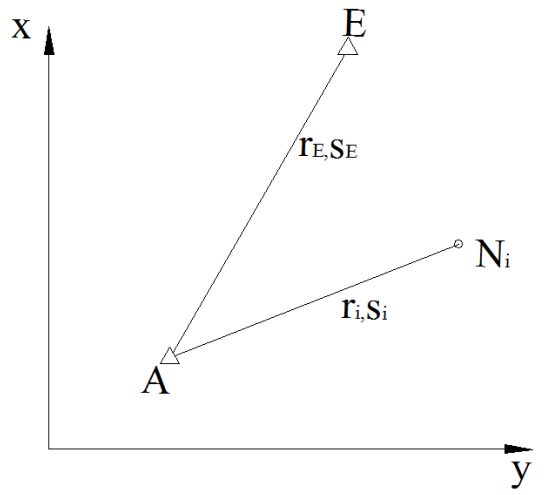

Figure 3.3.1: Principle of polar point calculation (following Kahmen [2006])

With the given coordinates of two points A and E, and the corresponding direction r_N and distance s_N the coordinates of point N can be calculated by (see [Kahmen, 2006]):

$$x_N = x_A + q s_N \cos(r_N + \varphi) \tag{3.3.1}$$

$$y_N = y_A + q s_N \sin(r_N + \varphi) \tag{3.3.2}$$

The orientation unknown φ is calculated as discribed in Section 3.1.
The scale factor q is calculated by determining at least one distance, i.e. s_{AE}:

$$q = \frac{s^{\star}_{AE}}{s_{AE}} \tag{3.3.3}$$

with

$$s^{\star}_{AE} = \sqrt{(x_E - x_A)^2 + (y_E - y_A)^2} \tag{3.3.4}$$

The scale factor q can be neglected if it is not significantly different to 1. The displacements of the masts have to be measured with an accuracy of $<1\,\text{mm}$. As the

longest distance measured between one total station and one of the prisms is 7.5 m a threshold value for the scale factor results

$$q_{min} = 7.501/7.5 = 1.0001$$

3.3.1 Accuracy of polar coordinate calculation

The Helmert position error of a polar point calculated from a known point is:

$$\sigma_p = \sqrt{(s \cdot \sigma_{r^0})^2 + \sigma_s^2} \tag{3.3.5}$$

where σ_{r^0} is the standard deviation of the oriented directions and s is the measured distance. $s \cdot \sigma_{r^0}$ gives the standard deviation lateral to the directional beam and σ_s the one in beam direction.

Usually one tries to use a setup where distance and angular accuracy are almost the same.

$$s \cdot \sigma_{r^0} = \sigma_s = \sigma_0 \tag{3.3.6}$$

The Helmert position error of the new point can then be calculated by:

$$\sigma_p = \sqrt{2}\sigma_0 \tag{3.3.7}$$

For distances s between 7.5 m and 1.8 m (see Section 4.3), standard deviations of the used total stations Leica TS30 of 0.6 mm+1 ppm in distance measurement and 0.15 mgon in direction measurement (see Section 4.1.1), a Helmert Position error of 0.6 mm emerges.

3.4 Orientation and base length calculation

The coordinates of the total stations in the local coordinate system and their orientation is known approximately. To obtain correct values for the coordinates of the prisms these values need to be known exactly. In Figure 3.4.2 the situation with three unknown parameters is shown. Usually one orientates two total stations by collimation. One points from one total station towards the rotational center of the other one and the other way round. In a second step all distances are scaled by a factor calculated with a reference bar. Collimation is not possible with the used Leica TS30 total stations, so other solutions for determining the exact values for the parameters B, O_1, O_2 had to be found. In this project a calibrated steel bar was used. Its length of $a = 1660.72mm$ has an accuracy of 1/100 mm. The bar was set up four times as shown in Figure 3.4.1 and the Hz- and V-reading from the total stations was done manually as the reference points were no prisms but marks on the bar.

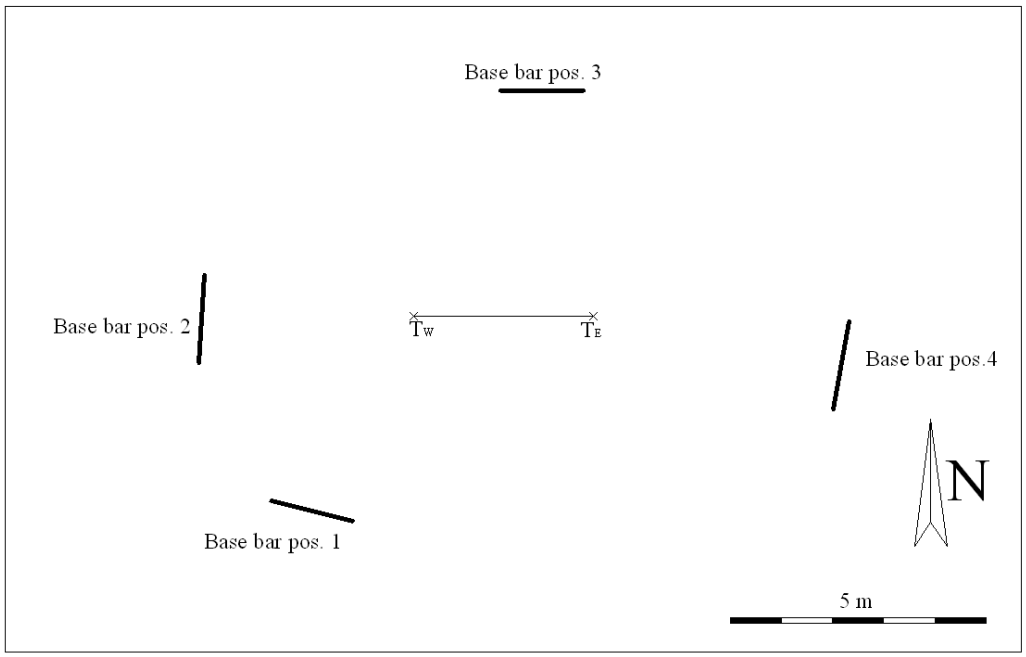

Figure 3.4.1: Ground view of base bar setup

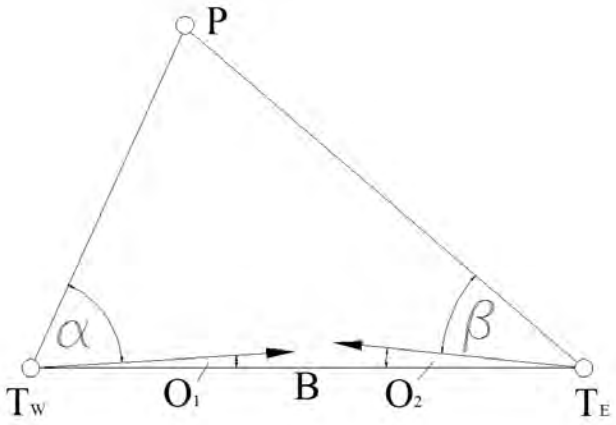

Figure 3.4.2: 2D-view showing the unknown parameters B, O_1, O_2 to determine

3.4.1 Calculation using the general case of a Least Square adjustment (LS-method)

The LS adjustment is a standard procedure and is based on minimizing the sum of the observal corrections squared

The general case in adjustment calculation (Niemeier [2008] and Navratil [2008a]) proceeds from an $(u, 1)$-vector of unknown parameters $\mathbf{X}$, an $(n, 1)$-vector of the ob-

servations $\mathbf{L}$ and functional relations $\mathbf{F}$ between them. The adjusted values for the unknown parameters and the observations are calculated using Equations 3.4.3 and 3.4.4.

$$\mathbf{L}_{(n,1)} \begin{bmatrix} L_1 \\ L_2 \\ \vdots \\ L_n \end{bmatrix} \; ; \qquad \mathbf{X}_{(u,1)} = \begin{bmatrix} X_1 \\ X_2 \\ \vdots \\ X_u \end{bmatrix} \tag{3.4.1}$$

$$\mathbf{F}(\mathbf{X}, \mathbf{L}) = \mathbf{0} \tag{3.4.2}$$

$$\hat{\mathbf{X}} = \mathbf{X^0} + \hat{\mathbf{x}} \tag{3.4.3}$$

$$\hat{\mathbf{L}} = \mathbf{L} + \mathbf{v} \tag{3.4.4}$$

In our case the observations are the azimuth values $r_{i,1}, r_{i,2}$ and zenith distance values $Z_{i,1}, Z_{i,2}$ from both total stations to eight points, so $n = 32$. The unknown parameters are the base length between the total stations B, the orientation error of both total stations O_1 and O_2, the height difference between the total stations dH and the coordinates of the eight measured points on the steel bar x_i, y_i, z_i, so $u = 28$. Between the unknown parameters and the observations 32 relations can be found by using equation types like the ones shown in 3.4.5:

$$\begin{aligned} F_{1,i}: &\quad \arctan\left(\frac{y_i}{x_i}\right) + O_1 - r_{1,i} = 0 \qquad i \in \{1, ..., 8\} \\ F_{2,i}: &\quad \arctan\left(\frac{y_i - B}{x_i}\right) + O_2 - r_{2,i} = 0 \\ F_{3,i}: &\quad \arctan\left(\frac{\sqrt{y_i^2 + x_i^2}}{z_i}\right) - Z_{i,1} = 0 \\ F_{4,i}: &\quad \arctan\left(\frac{\sqrt{(y_i - B)^2 + x_i^2}}{z_i - dH}\right) - Z_{i,2} = 0 \end{aligned} \tag{3.4.5}$$

Four more equations can be found by demanding that the distance between the four pairs of points for each setup of the steel bar is $a = 1660.72mm$ (see Equation 3.4.1).

$$F_j: \quad \Delta y^2 + \Delta x^2 + \Delta z^2 - a^2 = 0 \qquad (j \in \{1, 2, 3, 4\}) \tag{3.4.6}$$

First, one has to find approximations for the unknown parameters $\mathbf{X^0}$ and observations $\mathbf{L^0}$, such that Equation 3.4.7 is fulfilled.

$$\mathbf{F}\left(\mathbf{L^0}, \mathbf{X^0}\right) = \mathbf{0} \tag{3.4.7}$$

The model consists of n observations, u unknown parameters and b functional relations. In this case $n = 32$, $u = 28$, $b = 36$. The redundancy of the model is given by

$$f = b - u \tag{3.4.8}$$

and equals $f = 8$ in this model.

To solve the adjustment problem an (b, n) −matrix $\mathbf{B}$ consisting of the partial derivertives with respect to the observations, an (b, u) −matrix $\mathbf{A}$ consisting of the partial derivertives with respect to the unknown parameters and a $(b, 1)$ −vector $\mathbf{w}$ containing the discrepancies of the functional relations were set up.

$$\mathbf{w}_{(b,1)} = \mathbf{F}(\mathbf{L}, \mathbf{X^0}) = \begin{bmatrix} F_1(\mathbf{L}, \mathbf{X^0}) \\ F_2(\mathbf{L}, \mathbf{X^0}) \\ \vdots \\ F_b(\mathbf{L}, \mathbf{X^0}) \end{bmatrix} \tag{3.4.9}$$

$$\mathbf{B}_{(b,n)} = \frac{\partial \mathbf{F}(\mathbf{L}, \mathbf{X^0})}{\partial \mathbf{L}} = \begin{bmatrix} \frac{\partial F_1}{\partial L_1} & \frac{\partial F_1}{\partial L_2} & \cdots & \frac{\partial F_1}{\partial L_n} \\ \frac{\partial F_2}{\partial L_1} & \frac{\partial F_2}{\partial L_2} & \cdots & \frac{\partial F_2}{\partial L_n} \\ \vdots & \vdots & \ddots & \vdots \\ \frac{\partial F_b}{\partial L_1} & \frac{\partial F_b}{\partial L_2} & \cdots & \frac{\partial F_b}{\partial L_n} \end{bmatrix} \tag{3.4.10}$$

$$\mathbf{A}_{(b,n)} = \frac{\partial \mathbf{F}(\mathbf{L}, \mathbf{X^0})}{\partial \mathbf{X^0}} = \begin{bmatrix} \frac{\partial F_1}{\partial X_1^0} & \frac{\partial F_1}{\partial X_2^0} & \cdots & \frac{\partial F_1}{\partial X_u^0} \\ \frac{\partial F_2}{\partial X_1^0} & \frac{\partial F_2}{\partial X_2^0} & \cdots & \frac{\partial F_2}{\partial X_u^0} \\ \vdots & \vdots & \ddots & \vdots \\ \frac{\partial F_b}{\partial X_1^0} & \frac{\partial F_b}{\partial X_2^0} & \cdots & \frac{\partial F_b}{\partial X_u^0} \end{bmatrix} \tag{3.4.11}$$

The linearized functional model can now be expessed as:

$$\mathbf{B}\,\mathbf{v} \;+\; \mathbf{A}\,\hat{\mathbf{x}} \;+\; \mathbf{w} \;=\; \mathbf{0} \tag{3.4.12}$$

$\mathbf{v}$ is the vector of the corrections of the observations and $\hat{\mathbf{x}}$ the vector of the corrections of the unknown parameters. $\mathbf{v}$ can be calculated using equation 3.4.13 and $\mathbf{k}$ is called the vector of the correlatives.

$$\mathbf{v} = \mathbf{Q_{ll}}\mathbf{B^T}\mathbf{k} \tag{3.4.13}$$

$\mathbf{Q_{ll}}$ is called the cofactor matrix and is related to the covariance matrix by the variance factor σ_0^2. It applies

$$\mathbf{\Sigma_{ll}} = \sigma_0^2 \cdot \mathbf{Q_{ll}} \tag{3.4.14}$$

All measurements have the same accuracy of 0.5" and therefore cause an identity matrix for $\mathbf{Q_{ll}}$.

The normal equation matrix equals

$$\begin{bmatrix} \mathbf{BQ_{ll}B^T}_{(b,b)} & \mathbf{A}_{(b,u)} \\ \mathbf{A^T}_{(u,b)} & \mathbf{0}_{(u,u)} \end{bmatrix} \begin{bmatrix} \mathbf{k}_{(b,1)} \\ \hat{\mathbf{x}}_{(u,1)} \end{bmatrix} = \begin{bmatrix} -\mathbf{w}_{(b,1)} \\ \mathbf{0}_{(u,1)} \end{bmatrix} \tag{3.4.15}$$

If the normal equation matrix is invertable, $\hat{\mathbf{x}}$ and $\mathbf{k}$ can be calculated using

$$\begin{bmatrix} \mathbf{k}_{(b,1)} \\ \hat{\mathbf{x}}_{(u,1)} \end{bmatrix} = - \begin{bmatrix} \mathbf{BQ_{ll}B^T}_{(b,b)} & \mathbf{A}_{(b,u)} \\ \mathbf{A^T}_{(u,b)} & \mathbf{0}_{(u,u)} \end{bmatrix}^{-1} \begin{bmatrix} \mathbf{w}_{(b,1)} \\ \mathbf{0}_{(u,1)} \end{bmatrix} \tag{3.4.16}$$

3.4.2 Calculation using the Least Median Square adjustment (LMS-method) and the Newton iteration method

The LMS adjustment is a robust adjustment and is based on minimizing the median of the corrections of the observations squared.

$$med\left(v_i^2\right) \rightarrow min \tag{3.4.17}$$

With this method one calculates all possible unique solutions for the unknown parameters. The main advantage is that almost 50% of all unique solutions for the unknown parameters can be grossly incorrect and the calculation gives still quite good results. One major disadvantage is the very extensive amount of calculations for a high number of observations.

First, one starts by determining all possible solutions for the unknown parameters in $\mathbf{X}$. For each set of parameters a vector of the corrections for all observations $\mathbf{v}$ is calculated.

$$\mathbf{v}_i = \hat{\mathbf{L}_i} - \mathbf{L}_i \tag{3.4.18}$$

After determining the median of the corrections of the observations squared for each unique solution of the unknown parameters, the set which has the least median is used.

The unique calculation to determine B, O_1, O_2 was realized by using the multidimensional Newton iteration method. This method is based on determining a zero point of a defined set of functions $\mathbf{F}(\mathbf{X})$.

The general formula of the multidimensional Newton iteration is given by:

$$\mathbf{X}_{m+1} = \mathbf{X}_m - \mathbf{J}\left(\mathbf{X}_m\right)^{-1} \mathbf{F}\left(\mathbf{X}_m\right) \qquad \left(\mathbf{X}_i \in \mathbb{R}^{ux1}\right) \quad (i \in \mathbb{N}) \tag{3.4.19}$$

$\mathbf{X}_m$ is the m-th iteration for calculating one zero point of the functions defined by $\mathbf{F}(\mathbf{X})$ and $\mathbf{J}\left(\mathbf{X}_m\right)$ is defined as the Jacobi-matrix, which is the matrix made up of the partial derivatives of $\mathbf{F}\left(\mathbf{X}_m\right)$ with respect to $\mathbf{X}_m$ and its dimension is $u \times u$.

$$\mathbf{J}(\mathbf{X}_m) = \frac{\partial \mathbf{F}(\mathbf{X}_m)}{\partial \mathbf{X}_m} = \begin{bmatrix} \frac{\partial F_1}{\partial X_{1,m}} & \frac{\partial F_1}{\partial X_{2,m}} & \cdots & \frac{\partial F_1}{\partial X_{u,m}} \\ \frac{\partial F_2}{\partial X_{1,m}} & \frac{\partial F_2}{\partial X_{2,m}} & \cdots & \frac{\partial F_2}{\partial X_{u,m}} \\ \vdots & \vdots & \ddots & \vdots \\ \frac{\partial F_b}{\partial X_{1,m}} & \frac{\partial F_b}{\partial X_{2,m}} & \cdots & \frac{\partial F_b}{\partial X_{u,m}} \end{bmatrix} \tag{3.4.20}$$

If a zero point does not exist, $\mathbf{J}(\mathbf{X}_m)$ is not invertible i.e. $rk(\mathbf{J}(\mathbf{X}_m)) < u$ or the approximation of the zero point of $\mathbf{F}(\mathbf{X})$ is not good enough, the method can give wrong or no results. In this calculation a Jacobian matrix of rank 3 emerges of the parameters B, O_1 and O_2.

The conditional equations to set up the Jacobi matrix for calculating B, O_1 and O_2 can be found with the coordinates calculated with a forward intersection. The coordinates x_i, y_i, z_i of the points on the base bar are not necessary and do not take part in the calculation. They are presented here to explain how the conditional equations are made up.

$$x_i = \frac{B \cdot \sin(\beta_i + O_2)}{\sin((\alpha_i + O_1) + (\beta_i + O_2))} \cdot \sin(\alpha_i + O_1) \tag{3.4.21}$$

$$y_i = \frac{B \cdot \sin(\beta_i + O_2)}{\sin((\alpha_i + O_1) + (\beta_i + O_2))} \cdot \cos(\alpha_i + O_1) \tag{3.4.22}$$

$$z_{i,1} = \frac{B \cdot \sin(\beta_i + O_2)}{\sin((\alpha_i + O_1) + (\beta_i + O_2))} \cdot \cot Z_{i,1} \tag{3.4.23}$$

$$z_{i,2} = \frac{B \cdot \sin(\alpha_i + O_1)}{\sin((\alpha_i + O_1) + (\beta_i + O_2))} \cdot \cot Z_{i,2} \tag{3.4.24}$$

$$dH = z_{i,1} - z_{i,2} \tag{3.4.25}$$

Two different types of conditional equations were formulated:

- the height difference between the total stations dH calculated by measurements to two different points P_j and P_k has to be the same.

$$F: \ (z_{j,1} - z_{j,2}) - (z_{k,1} - z_{k,2}) = 0 \tag{3.4.26}$$

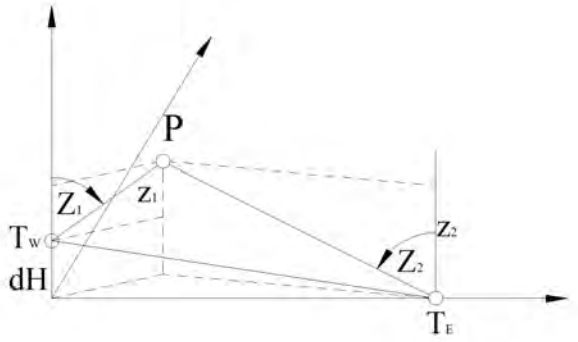

Figure 3.4.3: Conditional equations of type 1: the height difference dH between the total stations has to be constant (3D)

- the calculated length between two points on the base bar P_j and P_k has to be the known length of the bar of L =1660.72 mm.

$$F: \sqrt{(x_j - x_k)^2 + (y_j - y_k)^2 + (z_j - z_k)^2} - L = 0 \tag{3.4.27}$$

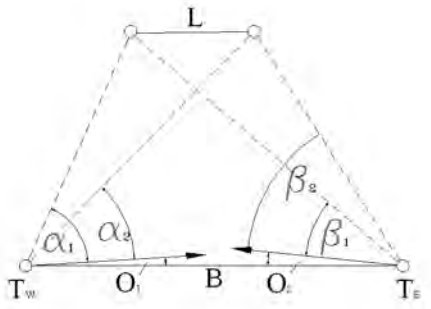

Figure 3.4.4: 2D-view of the principle of conditional equations of type 2: the length of the base bar is known

By plugging Equations 3.4.21 to 3.4.24 in Equations 3.4.26 and 3.4.27 the conditional equations can be found.

With four positions of the base bar eight points have been measured to. With those eight points it is possible to build seven linear independent equations of type one and four equations of type two. If there was no type two equation involved, the Jacobi matrix would become singular and no result would be found for that case.

The comparison of the results of both, the LMS- and the LS-adjustment showed that differences of only 0.3 mm in the base length and 2 mgon in the orientation error emerged. These values show, that no gross incorrect measurement was done. Without a gross error the results of the LS-method are usually more correct than the ones gained from the LMS-method, therefore the results of the LS-method were used for further calculations.

To make sure that the adjustment calculations were correct, the length between the rotational centers of the total stations was controlled using a laser tracker of type Leica Absolute Tracker AT901. It turned out that the calculated distance differed from the measured one by just 0.1 mm.

Chapter 4

Measurements

4.1 Used equipment

To realize the project, the following measurement instruments and equipment were used.

- two total stations Leica TS30
- six mini prisms Leica GMP104
- five ball prisms Leica RFI
- four metal temperature sensors
- two air temperature sensors
- one star pyranometer

The equipment is discussed in the following subsections.

4.1.1 Leica TS30

Figure 4.1.1: Leica TS30 total station

The used Leica TS30 total stations are highly accurate measurement instruments with accuracy values shown in Table 4.1.1 (see [Zogg et al., 2009]). They fulfill the demands of the project to detect displacements of at least 1 mm completely. They work with motorized drives based on the Piezo technology, as well as automatic target recognition (ATR), which works by calculating a centroid, is available. The total stations use a beam of light, which is reflected by the prism. The direction the total stations compute, is the centroid of the reflected portion of the beam. Logically the small Leica RFI prisms (see Section 4.1.3) used in this project reflect less light and energy than the Leica GMP104 prisms (see Section 4.1.2) with larger surfaces. The accuracy of the direction to the computed centroid of a beam is dependent on the amount of energy that is reflected. The less energy is reflected, the less accurate the computed direction to the centroid is.

Table 4.1.1: Leica TS30 properties Zogg et al. [2009]

Angle Measurement		
	Hz,V	0.5" (0.15 mgon)
Accuracy	Display Resolution	0.01" (0.01 mgon)
	Method	
Distance Measurement (Prism)		
Range	Round prism (GPR1, GMP104, RFI)	3500 m
	360° PRISM (GRZ4)	1500 m
	Reflective tape (60 mmx60 mm)	250 m
Accuracy/Measurement time to prism	Precise	0.6 mm+1 ppm/typ.7 s
	Standard	1 mm+1 ppm/typ.2.4 s
	Fast	3 mm+1 ppm/typ.0,8 s
Accuracy/Measurement time to prism		1 mm+1 ppm/typ.7 s
Distance Measurement (no Prism)		
Range		1000 m
Accuracy/Measurement time		2 mm+2 ppm/typ.3 s
Motorization		
Max. acceleration and speed	Max. Acceleration	400 gon/s^2
	Rotational speed	200 gon/s
Method	Direct drives based on Piezo technology	
Automatic Target Recognition (ATR)		
Range ATR mode / LOCK mode	Round prism (GPR1, GMP104, RFI)	1000 m/800 m
	360° prism (GRZ4, GRZ122)	800 m/600 m
Method	Digital image processing	
General		
Telescope	Magnification	30x
	Focusing range	1.7 m - ∞
Environmental Specifications	Operating temperature	-20°C to +50°C
	Dust/water	IP54
	Humidity	95%, non-condensing

4.1.2 Leica mini prism GMP104

Figure 4.1.2: Leica mini prism GMP104

The GMP104 is one of Leica's special prisms of the professional 1000 series (see [Leica, 2010]). It is mounted on an L-bar and can be installed in any direction with two screws, for setting the horizontal and vertical orientation. It is a regular mini prism, where the prism itself has a prism constant of 17.5 mm. The prism constant with respect to the rotational center given in Table 4.1.2 with +8.92 mm results from the difference between the offset of the prism center to the rotational center R of 8.58 mm (see Figure 4.1.3) and the prism constant of the prism itself of 17.5 mm. As the reflection center is not in the rotation center the distance and direction is dependent on the pointing direction of the prism. In Table 4.1.2 the relative variations of the prism constant and the height of the prism are presented. By tilting the prism around the tilting or standing axis by 45° a deviation of the prism constant of +2.5 mm is reached. The error transverse to the viewing axis reaches up to 6.1 mm at a tilting angle of 45° around the tilting or the standing axis. Theoretically the highest relative variations would appear at the maximum possible tilting angle of 50°. Due to the fact that the measured direction and distance to such very highly tilted prisms are quite inaccurate, the values for the maximum reasonable tilting angle of 45° are presented. The sum of the prism constant given in Table 4.1.2 and the correcting relative offset due to inclination of the prism gives the right values for the prism constant and the lateral displacement. The correcting relative lateral (Δl) and longitudinal (Δd) offset is calculated with the tilting angle α using Equation 4.1.1.

As only relative deformations of the monuments have been requested, it was not necessary to use the corrected prism constant, therefore the standard value for the

prism constant of 17.5 mm was used for all Leica GMP104 prisms.

Table 4.1.2: Leica GMP104 properties
Leica [2000]

Leica prism constant	8.92 mm
Relative prism constant (prism tilt around the tilting axis or swiveled around the standing axis up to 45°)	+2.5 mm (caused by eccentricity of the reflection center)
axis height	60.0 mm
Height (prism tilt up to 45° around the tilting axis)	±6.1 mm (caused by the eccentricity of the reflection center)
acceptance angle	±50°

$$\begin{pmatrix} \Delta l \\ \Delta d \end{pmatrix} = 8.58 \cdot \begin{pmatrix} \sin(\alpha) \\ 1 - \cos(\alpha) \end{pmatrix} \tag{4.1.1}$$

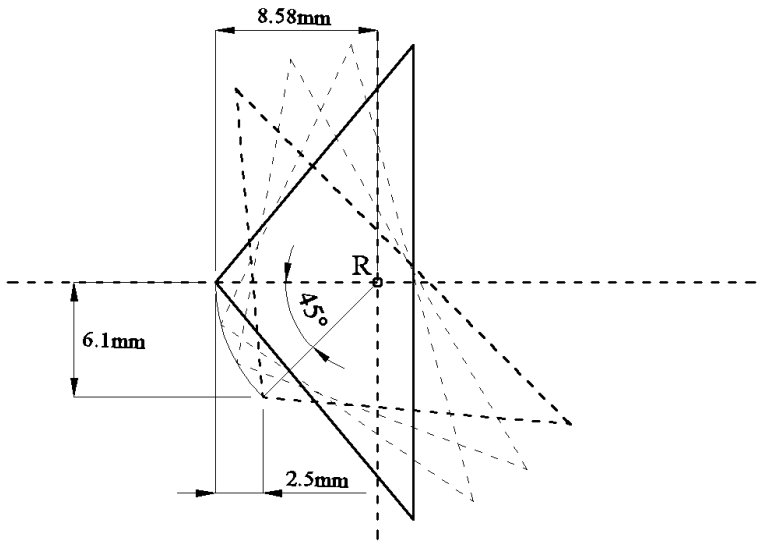

Figure 4.1.3: Relation between prism tilt and offset of the prism center with respect to the rotational center R.

4.1.3 Ball prisms Leica RFI

Leica RFI prisms are very small reflectors in the shape of a ball with a radius of 6.35 mm. RFI is the abbreviation of "Reflectors for Fixed Installations". As the center

of these prisms is given only roughly this type is only used for measuring coordinate variations. It is possible to glue them on many surfaces with hot glue to avoid complicated constructions to mount stable prisms on the object in question. Its surface is made of anodized aluminum and is therefore non-magnetic. The angle of acceptance is $\pm 50°$.

Figure 4.1.4: Leica RFI prisms

4.1.4 Star pyranometer

Figure 4.1.5: Star pyranometer (see [Fischer, 2005])

The Star Pyranometer is a basic instrument for measuring direct and diffuse solar radiation (global radiation). The sensing element is composed of twelve wedge-shaped thin copper sectors arranged radially, six white ones alternating with six black ones. When the sensor is exposed to solar radiation, a temperature difference is created between the black and white sectors. This temperature difference is proportional to the radiation intensity and is not affected by ambient temperature. Chromed constantan thermocouples are embedded in each sector to produce a 72 junction thermopile. Output from the

thermopile is approximately $15\mu V/Wm^{-2}$. The white sectors of the sensing element are painted with a special white paint that yields an almost perfect reflective surface. The black sectors are painted a highly absorbent flat black. The windshield that protects the sensor is a 2.75" diameter, polished crystal glass dome which admits electromagnetic radiation between 0.3 and 3 μm wavelength. The highly reflective outer surface, along with the mass of the case, keeps the case interior at ambient temperature. Instrument leveling is accomplished by means of a bull's-eye level and three leveling feet. When used in combination with an optional shadow band, the star pyranometer will measure diffuse solar radiation. In this project only one pyranometer was used, which measured the sum of direct and diffuse radiation. By using two star pyranometers total radiation can be seperated into direct and diffuse radiation. One pyranometer, with a shadow band, to measure diffuse radiation and a second one, without the shadow band, to measure both direct and diffuse need to be installed. The difference between the two measurements is direct radiation.

4.1.5 Temperature sensor read-out with Picotech Pico Logger PT-104

The Pico Logger PT-104 is a four-channel temperature measuring data logger with a measuring accuracy of 0.01°C. It can also be used to measure resistance and voltage. For this project the temperature sensors have been placed on several positions (see Chapter 5.1). As only four channels are available some sensors had to be replaced during the measurement period.

4.2 Timetable

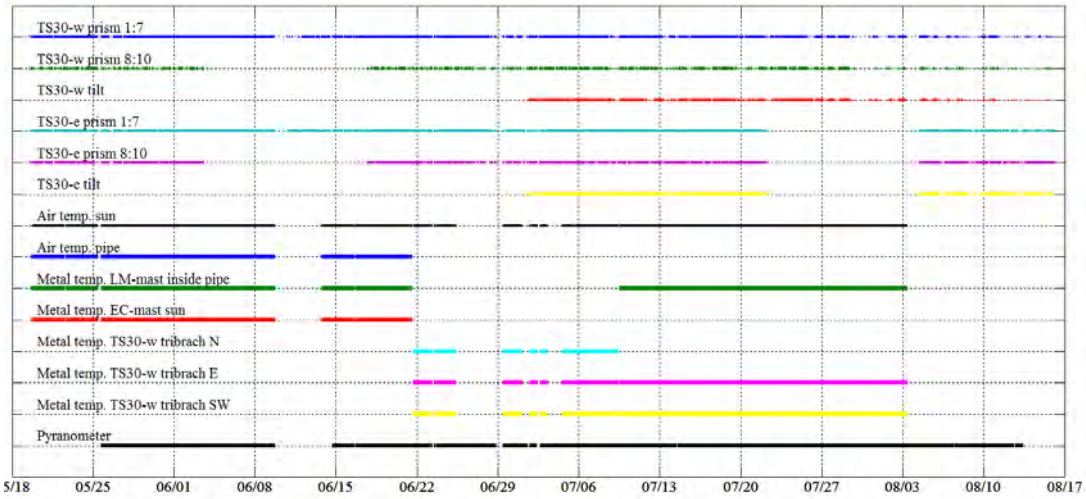

Figure 4.2.1: Measurement timetable from 05/19/2010 till 08/16/2010

In Figure 4.2.1 a time table about the measurements of all instruments used in this thesis is presented. Prisms 1:7 are the ones at the top of all four masts and the three ones on the ground to monitor the orientation of the total stations (line 1 and 4 in Figure 4.2.1). Prisms 8:10 are the ones at the bottom of the LM-mast for monitoring the tilt of the mast (line 2 and 5 in Figure 4.2.1). Additionally the tilt values of the total stations were read out to see the effect of solar radiation on the deformation of the total stations (line 3 and 6 in Figure 4.2.1). On lines 7 to 13 the temperature sensors on several places, as in the sun, in the shade, in the air, at the masts and at the tribrach of the total stations west, are shown. On the last line the time, when the pyranometer measured solar radiation, is shown.

The deformation measurements to the masts were carried out under several different conditions. The LM-mast was analyzed with and without the protective pipe, and additionally as an air circulated and a non-air circulated structure. Due to the fact that under non-air circulated conditions all holes in the bottom part had to be closed, it was not possible to measure the prisms at the bottom part of the LM-mast from 06/03 till 06/17 (see lines 2 and 5 in Figure 4.2.1).

Due to a software problem the compensator readout started only on 07/01 (see line 3 and 6 in Figure 4.2.1). The compensator was activated for all measurements.

All measurements from the eastern total station stopped on 07/22 suddenly. After solving the problem the total station was started again on 08/04. It is viewable that the western total station had many problems during the last three weeks of the measurement period. One reason can be that the drives were fouled by dirt or dust.

Several temperature sensor positions have been used for the analysis. Due to the fact that there have been just four input slots for the temperature sensors, it was necessary to confine oneself to four sensors at the same time. A schedule was created to cover all sensor positions. (see lines 7 to 13 in Figure 4.2.1, at no time were there more than four sensors recording).

The air temperature has been stored for all time, because it is the most important one of all temperature sensor positions.

In the first part of the temperature data collection, the air temperature inside and outside the protective pipe, the metal temperature of the LM-mast and the metal temperature of the sunny side of the EC-mast have been stored.

The second temperature measuring part started on 06/21 where only the air temperature sensor outside the pipe was not removed. The remaining three slots were used for three temperature sensors which were mounted around the tribrach of the western total station to be able to analyze the relation between the compensator readout and the temperature gradient inside the tribrach. That was accomplished by distributing the sensors equally around the tribrach. After two and a half weeks, on 07/10, one of the tribrach sensors was replaced by the metal temperature sensor on the LM-mast.

On 08/02 the temperature sensors had to be removed and given back to SP Technical Research Institute of Sweden (see Section A.2.1). The pyranometer recorded all the time. There was one power failure on 06/09. After remedying some hardware problems all measurement worked fine on 06/14 again.

4.3 Measurement setup

The system was set up at Onsala Space Observatory on stable bedrock. To ensure good calculation conditions the positions of the masts and total stations have been chosen in such a way that the angles inside the triangles between the two total stations and each mast are not too sharp. Figure 4.3.1 gives an overview of the system. The maximal distance is 7.5 m and the minimal distance is 1.8 m.

Three prisms distributed equally around the total stations were mounted directly on the bedrock to control the orientation of the total stations constantly. Due to the fact that the area on which the system was built up was not homogeneously covered with stable bedrock, the ground prisms had to be mounted that close to the total stations. As described in Chapter 5.4, one of those three prisms gave strange measuring results and therefore was not used for the calculations. With two remaining prisms it was still possible to find faulty measurements and even out orientation errors properly. The total stations were mounted directly on bedrock to ensure stability. The movement in height due to thermal expansion of the construction (see Figure 1.1.2) was very low, as the steel screws reached only a few centimeters out of the bedrock. If the total stations were mounted on tripods, it was not possible to stabilize them accurate enough. Also wind forces on the construction were much higher and thermal expansion resulted in much greated errors in height. Solar radiation acting on the total stations heated them up asymmetrically as one side was in the shade. The temperatures difference between the sun- and the shade side of the total stations resulted in bending effects. As the total stations work with an compensator the tilt did not falsify the direction measurements. The error of the position of the reference points of the total stations was negligible with maximally 0.07 mm. Dust and dirt became a problem in the end of the measurement period as the drives ceased working effectively. One more disadvantage that came up with the construction on the bedrock was the effect of refraction. The beam passes layers of air with different density values due to different temperatures. It is bent on the way through the air and therefore an error in the direction measurements occurs. As the horizontal temperature gradient is almost zero the effect of refractions takes place in height mainly. In Chapter 7 it is presented how the air temperature is related to the vertical displacement. The theoretical expansion coefficient is known and fits well to the measured values, one can see that the error due to refraction is not significant. The chosen solution for mounting the total stations on the bedrock would not have been possible in winter, when snow could have covered the instruments. The crosses in Figure 4.3.1 symbolize the ground prisms with numbers 1 to 3, the circles are the prisms at the top of the masts with numbers 4 to 7 and the triangles symbolize the total stations east and west.

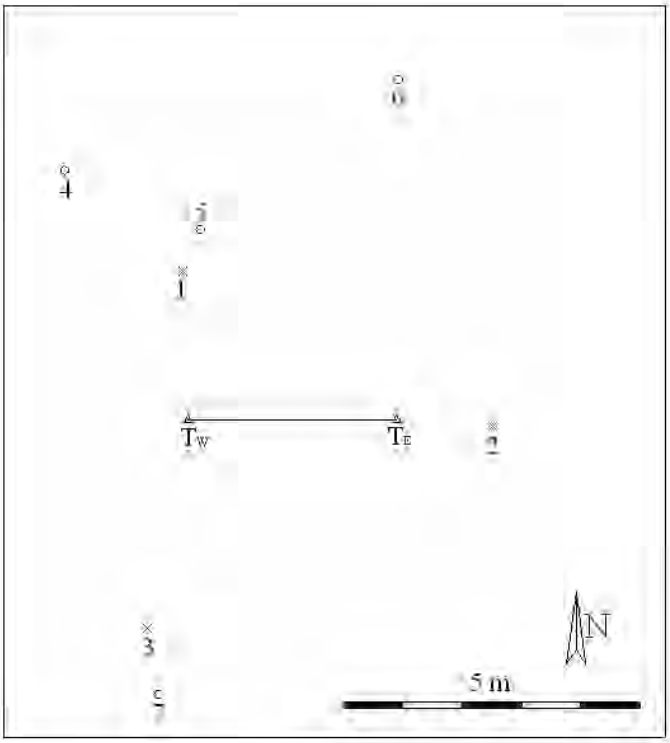

Figure 4.3.1: 2D-view of mast, prism and total station-setup

Chapter 5

Data Analysis

5.1 Temperature analysis

Several temperature sensors were set up to be able to see dependencies between different temperatures and deformations of the monuments. The most important sensor was the one that measured the air temperature at a height of 1.50 m. Standard meteorolical stations all over Sweden measure air temperature continuously. If just the air temperature was enough to correct the GNSS-results properly, it would not be necessary to install sensors near or on each mast that is built up for the GNSS-measurements. It was necessary to mount the sensors not too close to the ground to avoid influences of the temperature differences between the bedrock and the air.

5.1.1 LM-mast with pipe

Figure 5.1.1 shows the air temperature values inside the pipe and in the sun outside the pipe recorded every minute from 05/23 to 05/30. Due to the holes, which were drilled at the bottom of the pipe, air circulation was assured. The temperature difference between those two temperature sensors was therefore very small. It takes some time for the temperature differences to become zero. The time delay of the temperature inside the pipe with respect to the temperature outside the pipe reaches up to 40 minutes. During such periods, temperature differences of up to 3°C were observed. Figure 5.1.2 is a zoom into Figure 5.1.1. It shows the time delay on 05/27 and 05/28. Additionally, the curve of the temperature inside the pipe is smoothed a little bit as small, short peaks are attenuated.

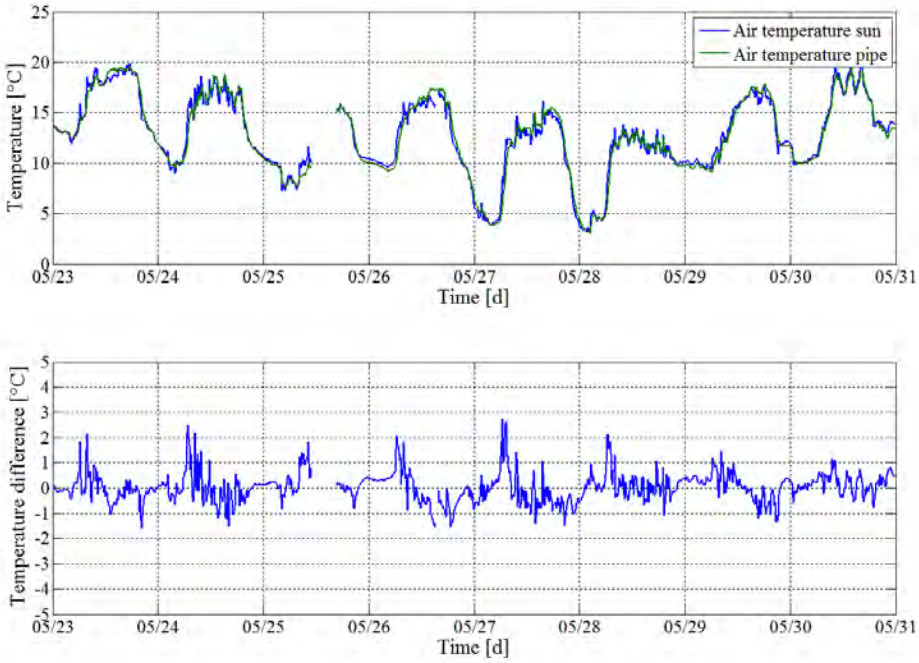

Figure 5.1.1: Temperatures (top) and temperature difference (bottom) of the air temperature inside and outside the pipe as an air circulated system

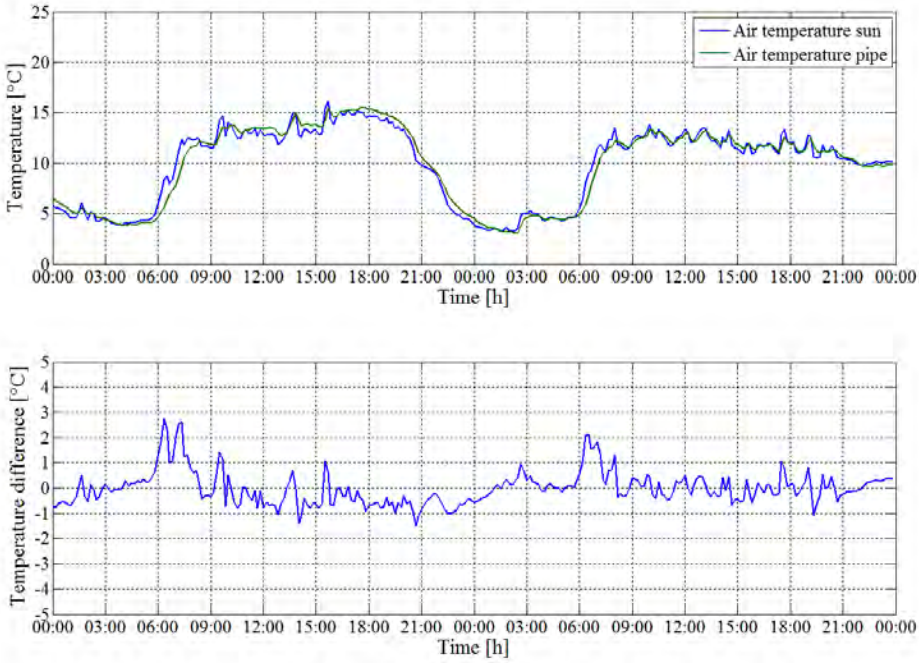

Figure 5.1.2: Zoom into Figure 5.1.1 from 05/27 till 05/28: time delay between temperature in- and outside the pipe is visible

On 06/03 the holes for air circulation in the bottom of the pipe surrounding the LM-mast were closed in order to investigate the mast as a non-air-circulated system. On sunny days the effect of solar radiation resulted in a constantly higher difference between the temperature inside and outside the pipe of approximately 3°C. On cloudy days and during the night there is almost no temperature difference. The temperature information in Figure 5.1.3 and the pyranometer readout in Figure 5.1.4 show that on the 06/07 and 06/08 there was very little solar radiation due to clouds and, therefore, the temperature was almost the same inside and outside the pipe.

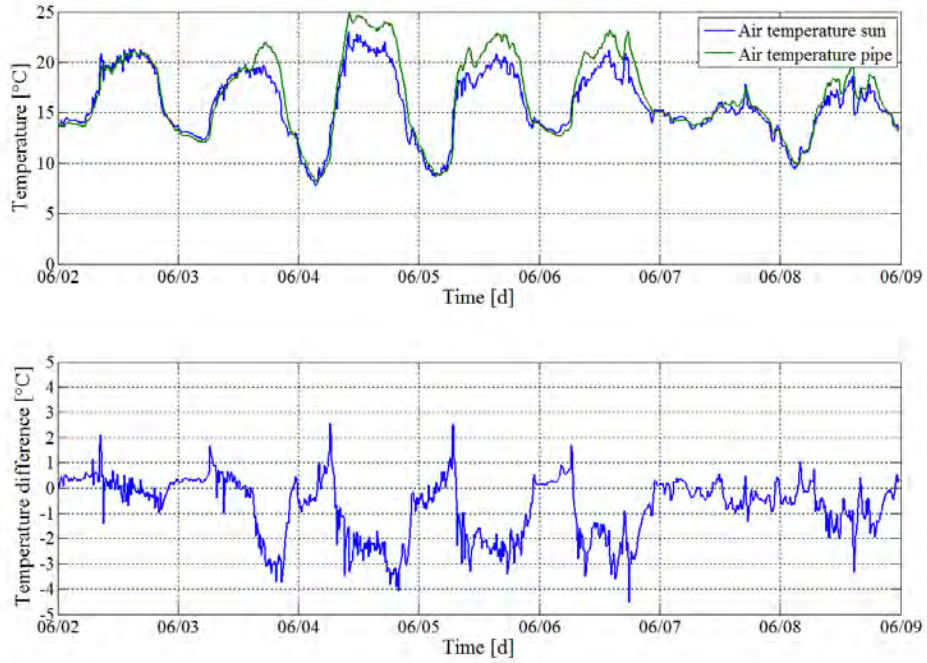

Figure 5.1.3: Time series of the temperatures inside and outside the pipe (top), and the temperature difference (bottom); Note: On 06/03 at 15:00 air circulation was stopped

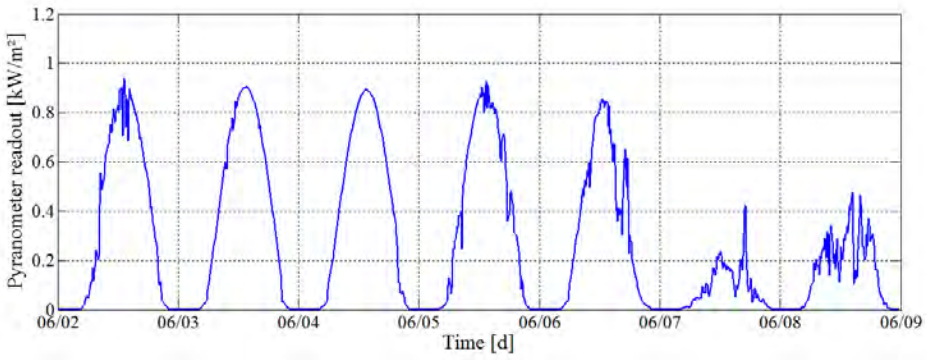

Figure 5.1.4: Solar radiation measured with pyranometer

The relevant temperature for heating up the LM-mast is the surrounding temperature inside the pipe. The difference of the metal temperature of the LM-mast and the air temperature inside the pipe is very small with 3°C at a max, and again there is a noticeable time delay as the warming and cooling of the metal needs some time. During heavy temperature rises and falls, the difference between the metal temperature and

the air temperature outside the pipe is quite high with up to 5°C (see Figure 5.1.5). It is accurate enough to use the air temperature outside the pipe to calculate the theoretical thermal expansion of the mast as a maximal error of 5°C would falsify the result with only 0.1 mm in height. It is recommended to use an air circulated system as it is very easy to realize by drilling holes and brings a slight improvement of the measurement results. The values measured by the standard meteorogical stations can be used for calculating the thermal expansion of the masts.

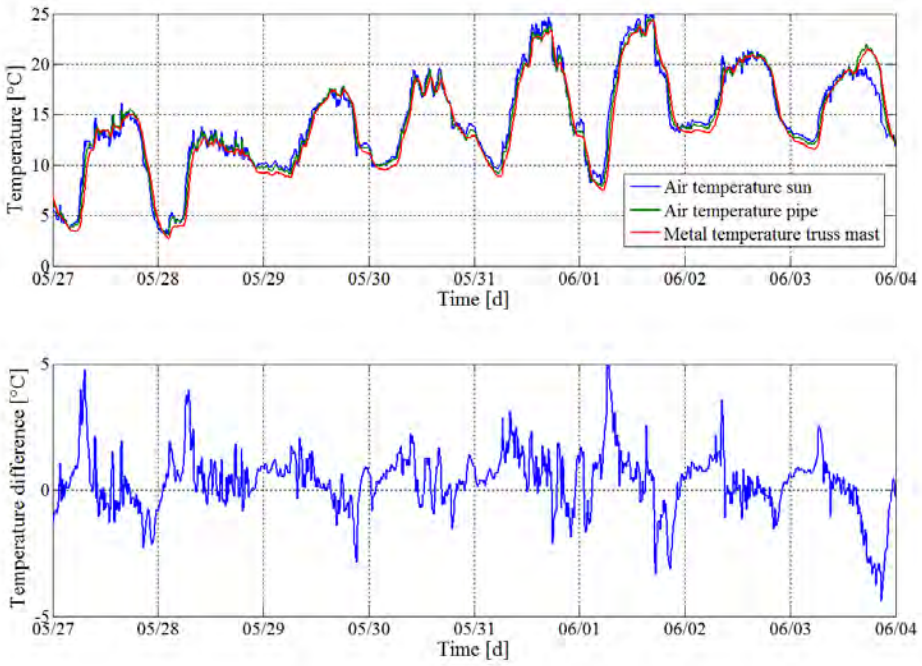

Figure 5.1.5: Top: air temperature in- and outside the pipe, and metal temperature of the LM-mast; bottom: difference between the metal temperature of the LM-mast and the air temperature outside the pipe

5.1.2 EC-mast and air temperature in the sun

The comparison between the air temperature and the temperature of the sunny side of the EC-mast shows that on sunny days (see Figure 5.1.4) the differences are quite high with up to 10°C (see Figure 5.1.6). As the expected error of the height expansion predicted using the air temperature instead of the actual steel temperature is up to 0.4 mm it is accurate enough to use the air temperature to calculate the height expansion.

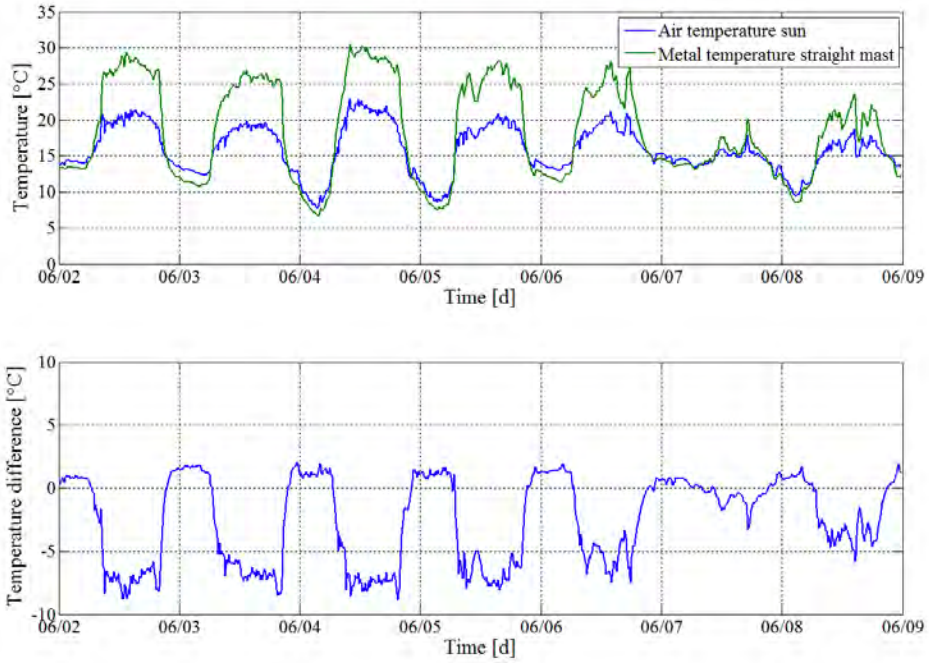

Figure 5.1.6: Time series of the temperature of the sunny side of the EC-mast and the air in the sun (top), and the temperature difference (bottom)

5.1.3 Comparison of the metal temperature - sun to shade

In Figure 5.1.7 the temperature graph shows that temperature differences of up to 10°C between the sunny and shady sides of the EC-mast can be reached. That is obviously dependent on the solar radiation intensity. On cloudy days the difference is much less.

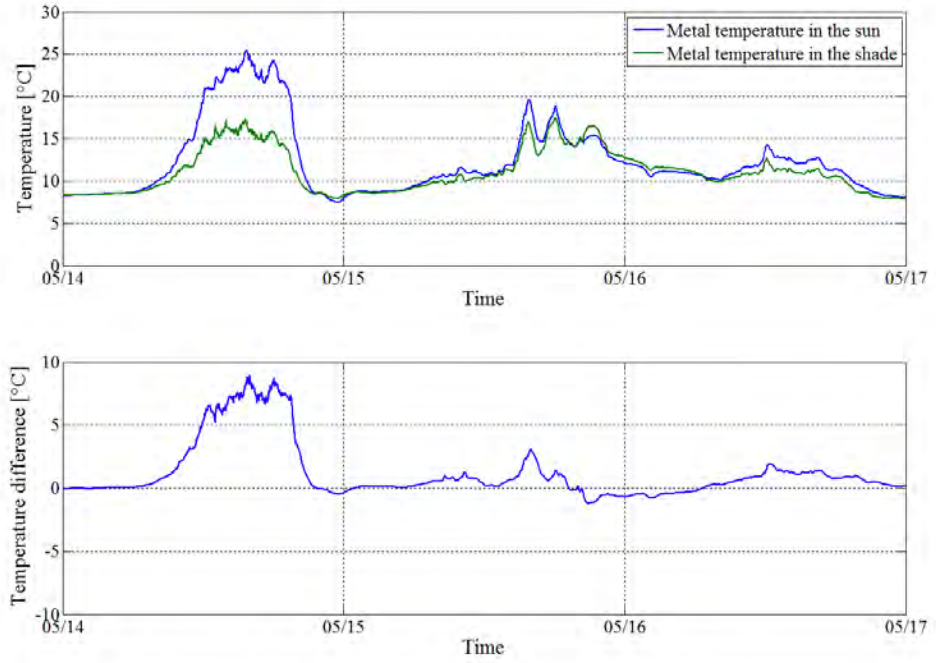

Figure 5.1.7: Time series of the metal temperature of the EC-mast in the sun and in the shade (top), and the temperature difference (bottom) from 05/14 till 05/16

5.2 Wind measurement results

The wind speed and direction was obtained from standard meteorological instruments at Onsala Space Observatory. During the whole project, wind speed values of up to 18 m/s were measured. Wind is a very dynamic force and has to be analyzed closely to find meaningful relations between the deformations of the masts and the wind forces. The measurement intervall to all prisms was 10 minutes. It would have been necessary to do the measurements at least once per second which was not possible with the used setup. In Figure 5.2.1 one can see that during the night from 05/24 to 05/25 the radial displacement of the EC-mast reached values up to 0.4 mm with an empirical standard deviation of 0.17 mm, although the wind was very strong with up to 18 m/s. By comparing the horizontal deformations during that night with the ones during windless nights, as e.g. the night from 05/21 to 05/22 with 0.06 mm empirical standard deviation and maximal radial displacements of 0.15 mm, one can see that the effect of wind to the deformation of the masts is neglectable for the accuracy demands of this project.

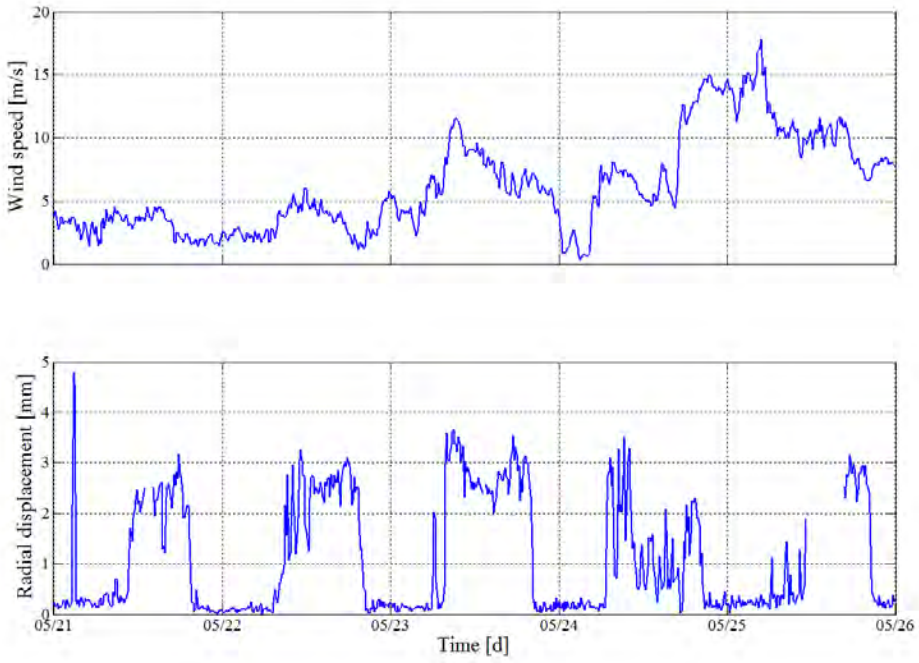

Figure 5.2.1: Time series of the wind speed and the radial displacement of the top prism of the EC-mast from 05/21 till 05/25

5.3 Orientation

It is very important to control the orientation of the total stations regularly to avoid systematic errors in the direction measurements to all prisms. That has been realized by three ground prisms that were mounted directly on the bedrock where they did not move. The orientation monitoring was carried out with only two prisms because of unaccountable measurement errors to the third prism (see Section 5.4).

In Figure 5.3.1 the change of orientation with respect to the beginning of the measurement cycle, measured from the western total station to ground prism one, is shown. A long term drift of about 3 mgon per month in one direction during the whole measurement period is readily identifiable. Additionally, there have been daily variations of about 5 mgon from peak to peak. These variations are likely due to refraction, solar radiation on the total stations, thermal expansion of the frame of the prisms, and so on. As those daily changes do not look the same with all ground prisms, the reason for the inconstant orientation is mainly due to deformation of the prism frames (see Figure 5.3.2). Figure 5.3.3 shows the directions of the prisms with respect to the value at 00:00 on 07/02 after application of the respective estimated orientation. As prism two was not used for the estimation, the direction has an higher standard deviation

with 1.3 mgon than the other two with 0.27 mgon and 0.4 mgon.

An error of 5 mgon would affect the calculated displacement by 0.8 mm over a distance of 10 m. The orientation was computed with an intervall of ten minutes over the whole measurement period of three months and was included in each epoch of deformation measurements.

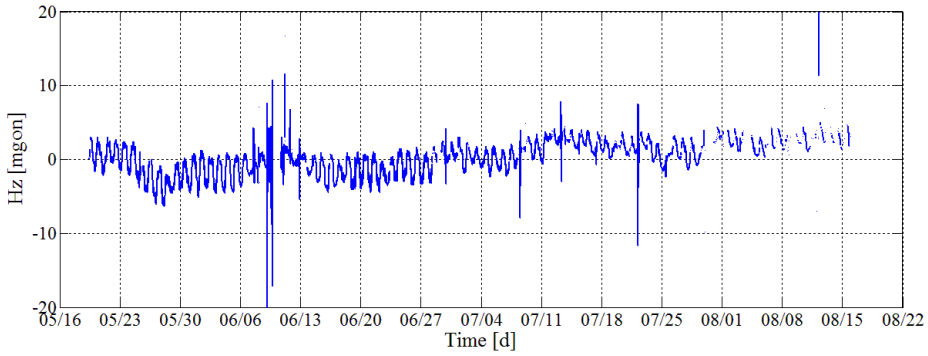

Figure 5.3.1: Horizontal direction with respect to the direction at the beginning of the measurement period from TS30 west to ground prism 1 (average of face 1 and face 2 readings without orientation correction)

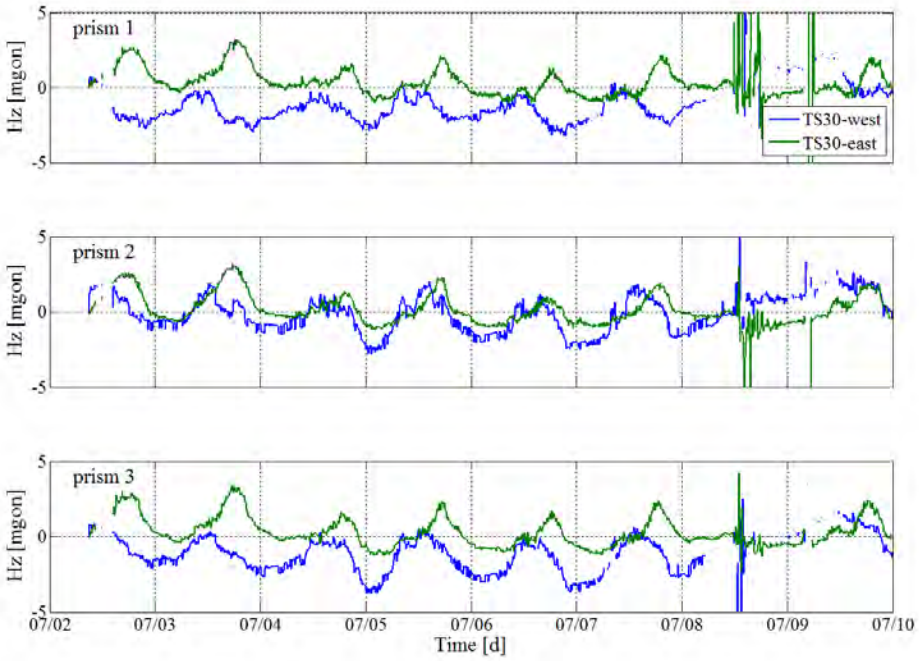

Figure 5.3.2: Horizontal directions with respect to the directions on 07/02 at 00:00 (average of face 1 and face 2 readings without orientation correction)

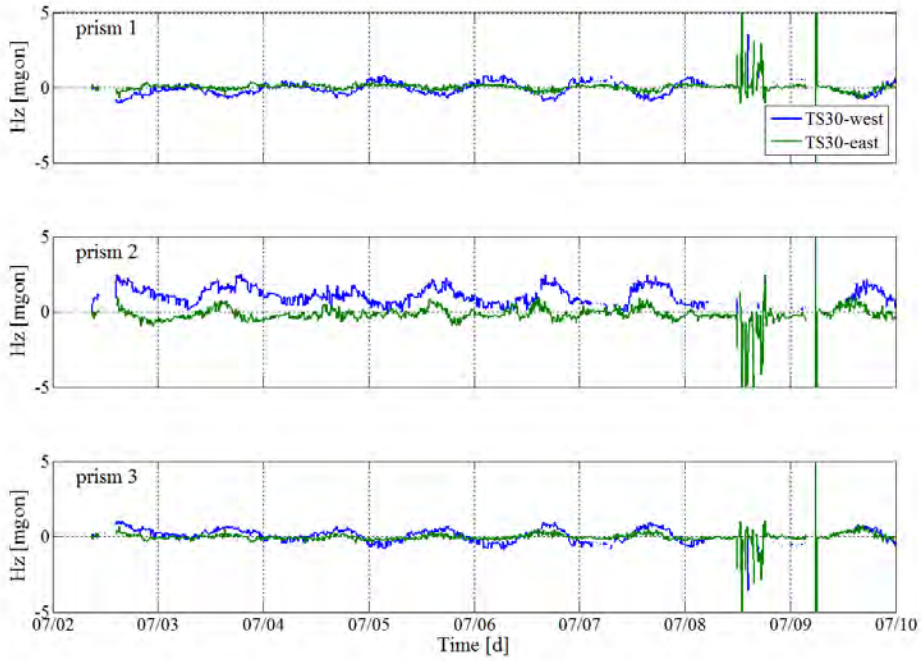

Figure 5.3.3: Horizontal directions with respect to the directions on 07/02 at 00:00 after application of the respective estimated orientation

5.4 Problems

5.4.1 Measurement errors

Unfortunately, there was a problem with one of the prisms mounted on the bedrock. On 05/28 there was an abrupt change in the horizontal readings from the western total station to one of the three ground prisms. As shown in Figure 5.4.1, the change took place in two steps by 0.01 gon and 0.04 gon. Neither of them can be seen in the measurements of any other prism or from the eastern total station of any prism at all (see Figures 5.4.2 and 5.4.3). There was no mechanical manipulation of the prism and the effect could not be reproduced by related experiments in the lab. During some days from 06/08 until 06/12 there were many strong rainfalls and thunderstorms that explain the strongly fluctuating measurements during that time. After those bad weather conditions, the position of the prism which moved unexpectedly was the same as in the beginning again for a short duration of two days from 06/12 till 06/13. In all likelihood there was an obstacle between the two total stations which affected the measurements from the western total station to the prism. The heavy rainfalls removed the obstacle and therefore the line of sight between the western total station and ground prism two was free again. That assumption cannot be clarified in hindsight.

The abrupt change of the Hz-measurements of prism two from both total stations (see Figures 5.4.1 and 5.4.3) on 06/14 is due to analyzing measurements which were carried out at ground prism two. The prism frame had to be loosened and was tightened again after the ivestigations. It was not possible to tighten it in the exact same direction as it was before, therefore that jump arised. Prism two was excluded from the orientation monitoring calculations and was then used for analyzing purposes. As there were two more ground prisms it was no problem to do the deformation calculations without ground prism two. The sudden drop of the Hz-measurements from TS30-east to all prisms on 06/16 is due to mechanical stress on the total station.

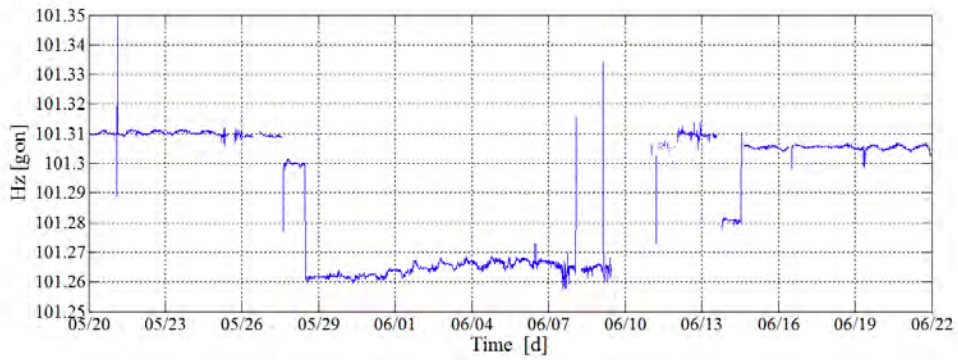

Figure 5.4.1: Hz-reading from TS30-west to prism 2

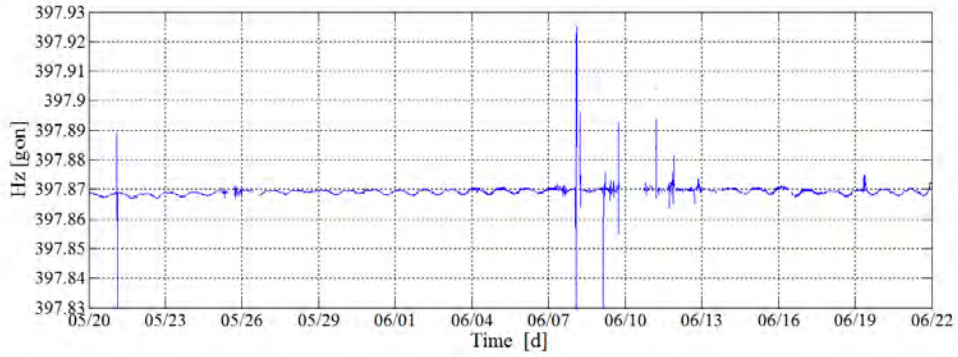

Figure 5.4.2: Hz-reading from TS30-west to prism 1

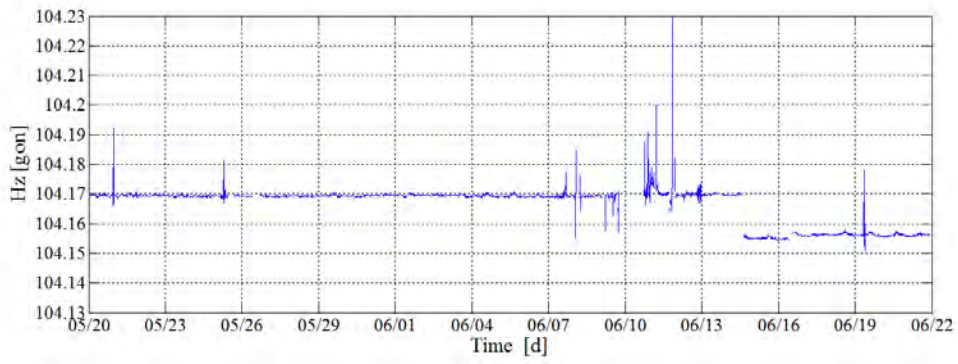

Figure 5.4.3: Hz-reading from TS30 east to prism 2

5.4.2 Accuracy of ball prisms

As the small ball prisms Leica RFI ("Reflectors for Fixed Installations") have a much smaller surface than the Leica GMP104 prisms, less energy is reflected. Thus the accuracy of the coordinates calculated with the Leica RFI prisms is much less, with 2.5 mgon, than with the Leica GMP104 prisms, with 0.3 mgon. From the reflected portion of the beam of light that is sent to the prism, the centroid is computed and gives the actual measurement value (see Section 4.1.1). The accuracy of the measured distances is the same with both types of prisms.

In Figure 5.4.4 the horizontal displacement of the truss mast top calculated by the tilt of the layer defined by the ball prisms at the truss mast bottom is presented. One can see that the calculation gives radial displacement values in the range between 0 and 8 mm. Outliers reach values of up to 1 m. The measured radial displacement values of up to 0.8 mm show that it is not reasonable to use the bottom prisms to calculate the tilt of the mast to be able to distinguish between bending and tilt of the mast.

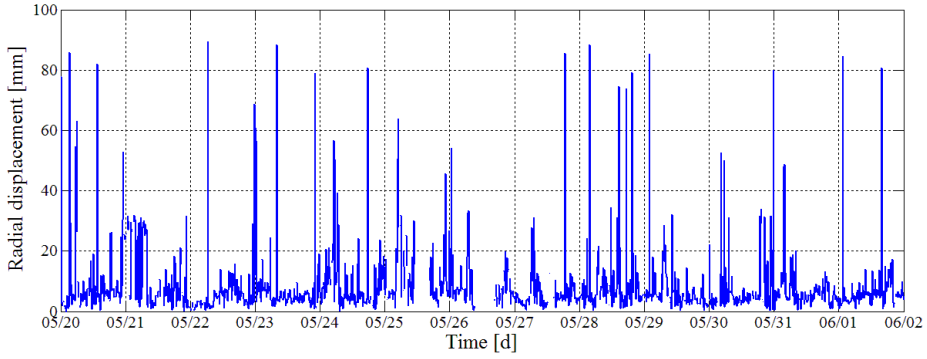

Figure 5.4.4: Time series of the displacement of the LM-mast top calculated by the ball prisms at the bottom of the mast

5.4.3 Tilt readout

Due to a software problem, storing the total station tilt measurements was not possible until the end of June. After solving the problem the readout could be started at the beginning of July. The compensators worked well all the time and the software problems did not influence the deformation measurements.

Chapter 6

Compensator functionality and readouts

6.1 Compensator used for the Leica TS30 total station

Within the Leica TS30 total station a very efficient type of compensator is used (see Zogg et al. [2009]). It can detect both, the longitudinal and transverse inclination using a single line sensor. This tilt sensor works in a range of 4' (0.07 gon) and has a setting accuracy of 0.5" (0.15 mgon).

The compensator mainly consists of a light source, a prism with a line pattern, a one-dimensional line sensor and an oil layer in a casing together with a prism and a mirror. The oil layer represents a surface that is perpendicular to the plumb line.

The priciple is shown in Figure 6.1.1. The LED-light source emmits a beam, which passes the prism with the line pattern. After being reflected by the oil layer and the mirror the line pattern is projected onto the CCD line sensor. The dual axis inclination can be inferred from the part of the line pattern projected onto the line sensor. This is visualized in Figure 6.1.2. Four parallel lines close to the center of the pattern always create an image with four equally spaced dark spots. Two tilted lines at either end create an image with two dark spots at either end. The distance between the centroids of the sets of spots is a measure of the transverse inclination. The position of the center of the pattern on the line sensor is a measure of the longitudinal inclination. Due to the very small construction of this compensator it is possible to mount it in the center of the total station. When rotating the total station, the liquid surface displacement of the oil and the settling time for the oil layer is then minimized.

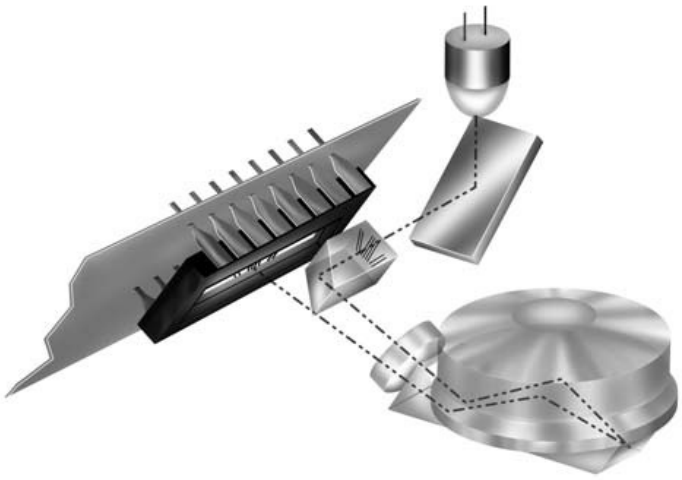

Figure 6.1.1: Principle of the dual axis inclination sensor (Zogg et al. [2009]).

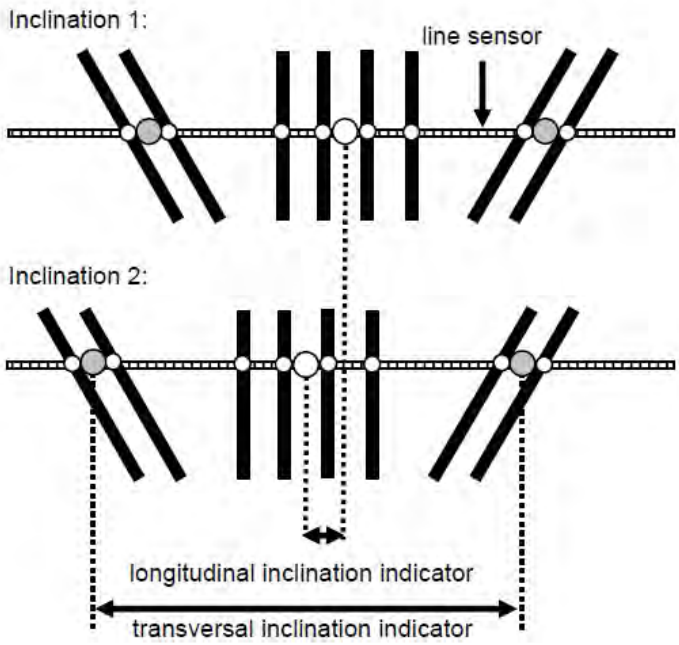

Figure 6.1.2: Line pattern for measuring longitudinal and transversal inclination by a single line sensor (Zogg et al. [2009]).

6.2 Readouts and correlation between sun-elevation, sun-azimuth and temperature

This investigation was done to improve the knowledge about the sensitivity of total stations with respect to solar radiation.

Figure 6.2.1 shows the relation between the position of the sun and the tilt readout of the western total station. The readouts give the tilt of the total stations and were made in two directions, transversal and longitudinal with respect to direction north. If the total stations were set up perfectly horizontally, tilting fromward the sun would be detected. As setting the horizontation cannot be made perfectly, the total station was already inclined before the sun and temperature differences affected it. Therefore, the tilt readout gave results which show that the tilt reached values between 10 and 20 mgon and the tilt direction of the total station was always only between 80° and 160°. It is visible that periodic deformations with an intervall of one day occured. The local extremes were measured during the morning and evening hours. Additionally, the daily maximum absolute tilt was measured during the evening when the sun is close to the horizon and the total station is almost tilted fromward the direction of the sun.

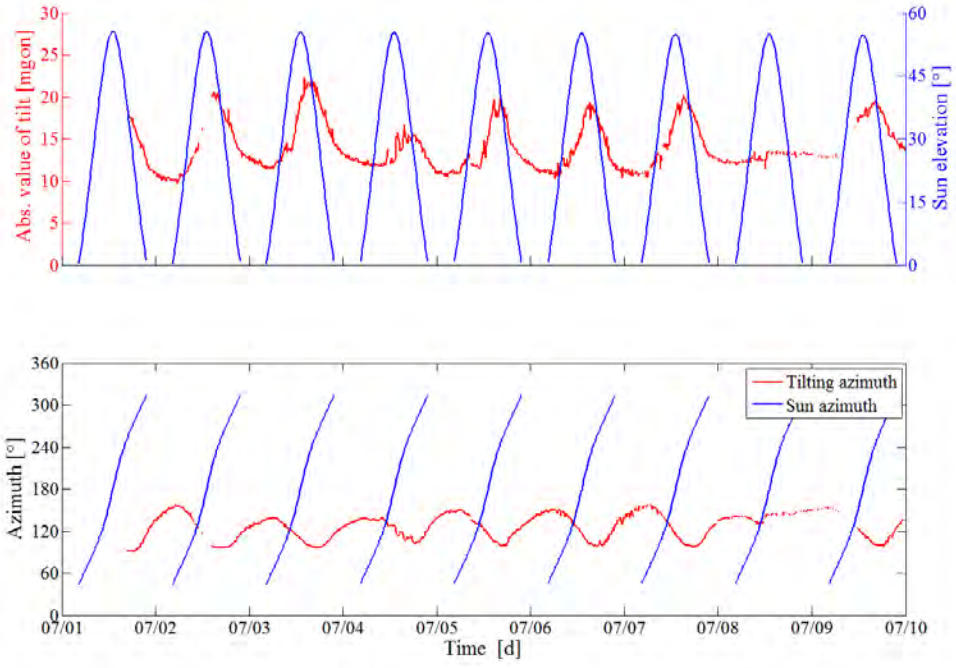

Figure 6.2.1: Time series of the sun elevation and the absolute value of the tilt (upper graph), and the azimuth of the sun and the tilting direction (lower graph) of the western total station.

To find the change of temperature inside the tribrach, three temperature sensors, distributed equally around the tribrach, were used. The differences of the measured values give the magnitude and direction of the temperature gradient. Figure 6.2.2 shows clear curves where during the day the temperature differences are quite high with of up to 10°C and the directions of the positive gradients point mostly towards the sun. During night time there are very small temperature differences, therefore the computed directions of the gradients are not accurate and should not be interpreted. Comprisingly one can say that solar radiation affects the total stations in terms of tilting and heating but these effects do not significantly falsify the results of the deformation measurements.

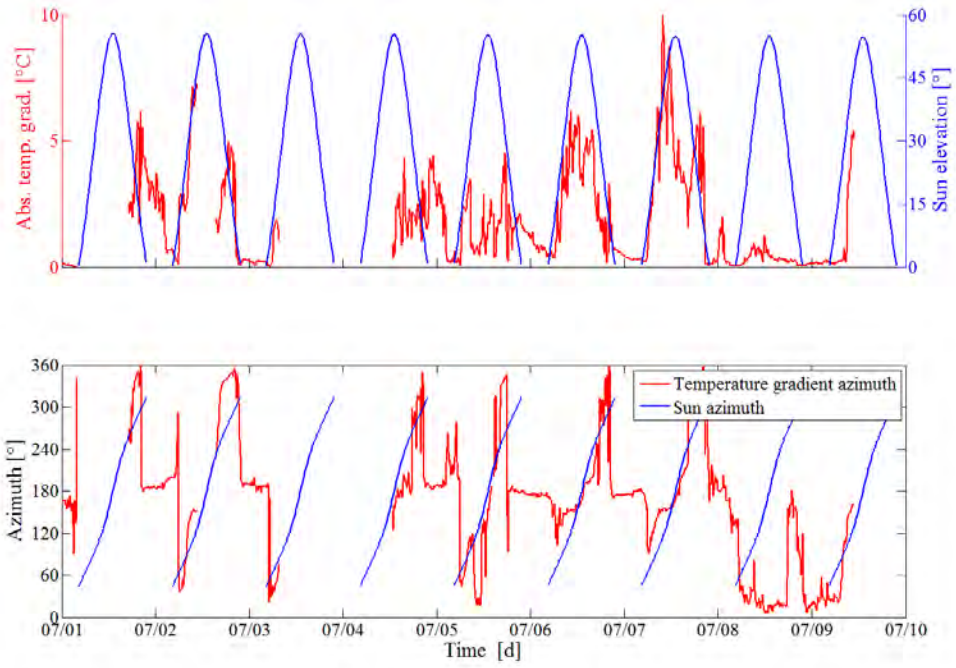

Figure 6.2.2: Time series of the sun elevation and the absolute value of the temperature gradient inside the tribrach (upper graph), and the azimuth of the sun and the temperature gradient direction (lower graph).

Chapter 7

Results

The monitoring of the deformations lasted three months and is based on a measurement interval of ten minutes. Movements due to solar radiation, temperature variations and wind were analyzed. Solar radiation gave the majority of all deformations. The software that was used to program the total stations was "Leica GeoMos".

The deformation behavior due to solar radiation gives mainly horizontal values. As the sunny and shady sides of the monuments have different temperature values, the masts deform horizontally because of non-symmetrical thermal expansion. Temperature variations cause vertical deformations.

As wind is a very dynamic force (see Section 5.2) it would have been necessary to increase the frequency of measurements up to at least one measurement per second to be able to correlate wind with deformations. Even on relatively windy days it was not possible to see any effect of the wind (see Section 5.2). During very rainy days the scattering increased with up to 200% which can be explained by reflection and refraction of the laser due to rain. One more reason for the scattering can be the vibrations of the masts due to the strong wind.

7.1 LM-mast

The LM-mast was analyzed under several different conditions.

- without the protective pipe
- with the protective pipe as a non-air-circulated system
- with the protective pipe as an air-circulated system

The use of the protective pipe around the LM-mast is necessary to avoid that people can climb on it. The investigations in the deformation of the mast under different conditions were done to increase the knowledge about that construction. The main interest was the investigation of the deformation of the LM-mast surrounded by the protective pipe. As the thermal expansion coefficient of the material that was used for

the LM-mast is with 7.5 ppm/K lower than the one of the other masts with 12 ppm/K the measurements results were adapted in Section 7.5 to be able to compare the results.

7.1.1 Without the protective pipe

Figure 7.1.1 shows the relation between the radial horizontal displacement of the prism at the top of the mast, the direction of the displacement (azimuth), the elevation and azimuth of the sun and the pyranometer readout from 06/24 until 06/28, when the pipe was not around the mast. During the night the radial displacements are very small and mainly due to measurement errors (see Figure 7.1.1). The calculated coordinates of the prism scatter around the mean of the positions between 2:00 and 3:00 in the morning. The reference coordinates were calculated for each night seperately. A threshold value for the radial displacement of 0.1 mm was used to distinguish between measurement errors and actual displacements. As the direction of the calculated displacement with respect to the reference coordinates results in very fluctuating values with radial displacements <0.1 mm these periods were grayed out. The displacements of up to 0.8 mm are very small in relation to the height of the mast with 3.2 m. In the morning of 06/27 the radial displacement is very low although the pyranometer shows much solar radiation. An explanation for that could not be found.

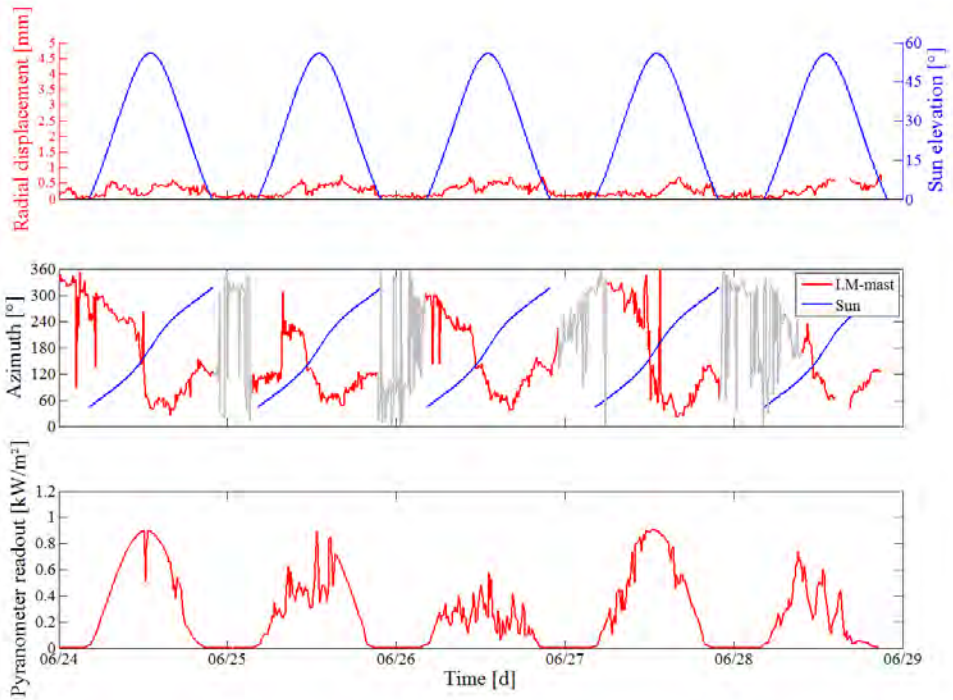

Figure 7.1.1: Time series of the sun elevation and radial displacement of the top prism of the LM-mast without the protective pipe (top), the sun- and displacement azimuth (middle), and the solar radiation measured with the pyranometer (bottom). (Values grayed-out during periods with radial displacements <0.1 mm)

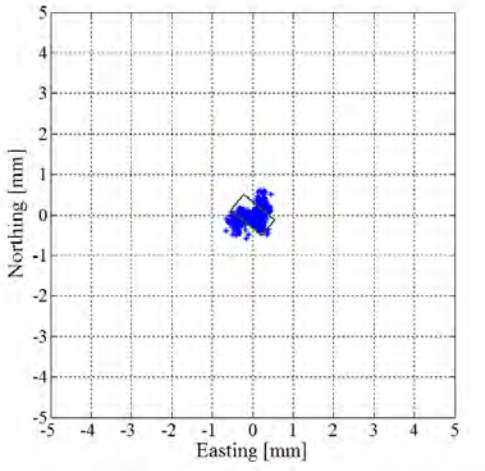

Figure 7.1.2: Horizontal deformation of the LM-mast without the protective pipe and the scaled cross section of the top part of the mast

06/25, 06/26 and 06/28 were relatively cloudy days as the graph of the pyranometer readout shows. On 06/24 and 06/27, some clouds covered the sky for short times.

The horizontal deformations are, as expected from the FEM-simulations (see Chapter 2), very small with up to 0.8 mm. All attracting forces affect the structure less than the other constructions as the solar radiation heats up all rods equally and the wind force is less on an open structure compared to a closed one. The only part that is heated up unsymmetrically is the one at the top of the LM-mast construction on which the GNSS-antenna is mounted.

The radial deformations have a peak in the morning and in the afternoon when the broad side of the top part is heated up by the sun. The majority of the deformation is due to the top part. Figure 7.1.2 shows the displacements of the prism at the top of the mast and the scaled cross section of the top part. It is visible that the deformations occur mainly in one direction, which is across the broad side of the top part. The scaled cross section of the top part of the mast is symbolized in Figure 7.1.2. This is comprehensible as a temperature difference between the sun and shade side of the top part causes higher deformations with narrower shapes as the temperature gradient is higher then.

At the bottom part of the mast three prisms were mounted to distiguish between tilt and deformation. The calculated layer defined by these prisms was not accurate enough to fit the demands of an accuracy of the pitch of the layer of 2 mgon and therefore was not used for further calculations.

7.1.2 With the protective pipe as an air-circulated system

This realization gives maximum deformation values of up to 0.6 mm which is only 0.2 mm less than the maximum of the construction without the pipe with 0.8 mm.

The basic advantage of the protective pipe is that people cannot climb on the truss construction and move the antenna by doing that. Additionally, the sun is blocked and does not deform the mast horizontally. The small horizontal movements shown in Figure 7.1.3 can be explained by the part mounted at the top of the mast which has a rectangular profile and reaches above the protective pipe. As that part is affected by the sun in both construction realizations and the maximum deformations reach almost the same values with a difference of 0.2 mm, it may be an indication that the lower truss construction gives those 0.2 mm deformations on the pipeless version.

Figure 7.1.3 shows that the main deformation takes place in the afternoon when the broad side of the mast top is heated up unsymmetrically. The almost constant azimuth in the afternoon shows that the deformation takes place in one direction, which is the one across the narrow side of the top construction.

In Figure 7.1.3 the magnitude of the horizontal deformation is shown. If the top part was also protected by a smaller additional pipe that reached directly under the GNSS-antenna, the deformations would presumably be much less. Again, as in the previous section, the direction of the displacements fluctuates very much (gray graph) when the magnitude of the displacement is small.

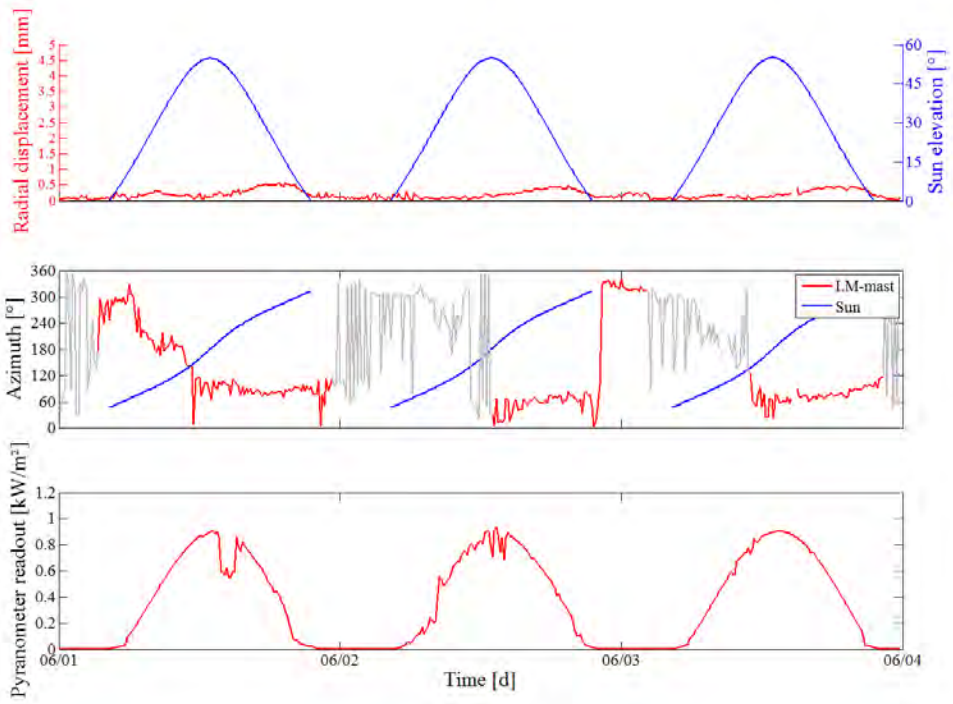

Figure 7.1.3: Time series of the sun elevation and radial displacement of the top prism of the LM-mast with the protective pipe as an aircirculated system (top), the sun- and displacement azimuth (middle), and the solar radiation measured with the pyranometer (bottom). (Values grayed-out during periods with radial displacements <0.1 mm)

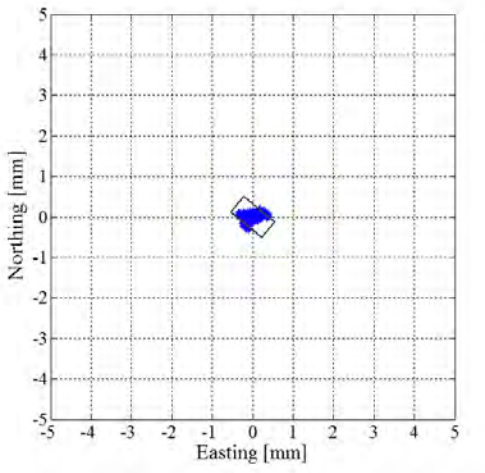

Figure 7.1.4: Horizontal deformation of the LM-mast with the protective pipe as an aircirculated system and the scaled cross section of the top part.

7.1.3 With the protective pipe as a non-air-circulated system

Closing the air circulating holes resulted in temperature differences between the air outside the pipe and the metal of the LM-mast of up to 5°C (see Section 5.1.1). Calculating the thermal expansion with the air temperature instead of the metal temperature causes an error in height of 0.1 mm.

Thermal expansion in height due to temperature variations acts, like in theory, linearly with 7.5 ppm/K. As Figures 7.1.5 and 7.1.6 show, a temperature variation of 35°C results in a change in height of the 3.20 m high mast of about 0.8 mm. The empirical standard deviation of the residuals of the mast height values calculated with the air temperature is 0.078 mm and calculated with the metal temperature 0.065 mm. The investigations of the temperature relations show that it is accurate enough to use the air temperature, which can be achieved from standard meteorological stations nearby the location, instead of the metal temperature. It is therefore not necessary to install an additional temperature sensor on each GNSS-monument.

During the whole measurement period temperatures between 2 and 30°C have been reached.

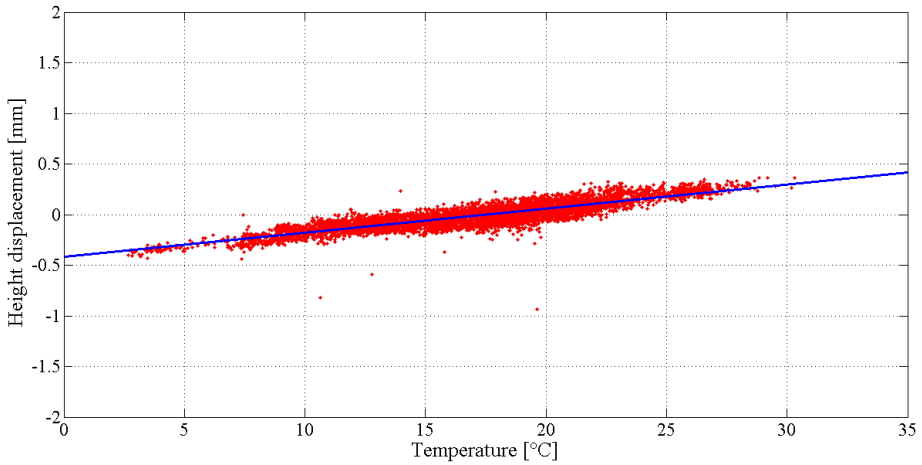

Figure 7.1.5: Relation between the metal temperature and the height displacement of the LM-mast with respect to the mean height value.

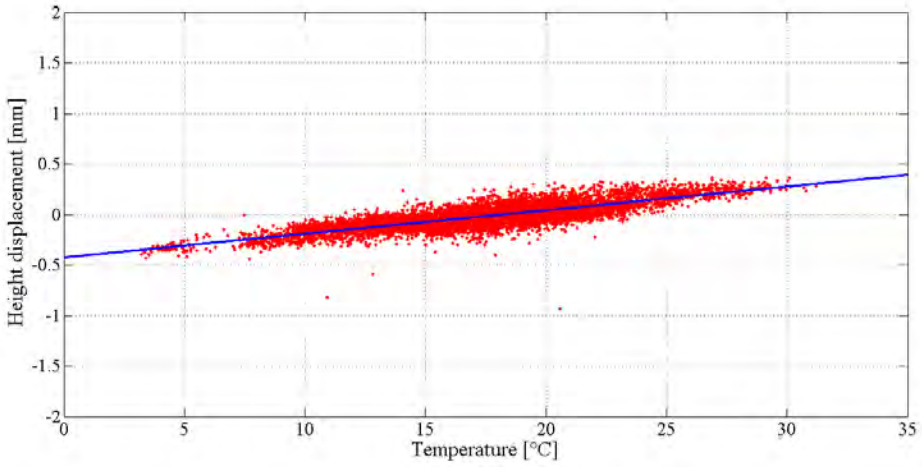

Figure 7.1.6: Relation between the air temperature and the height displacement of the LM-mast with respect to the mean height value.

Naturally, the comparisons of results under not exactly the same conditions are not as meaningful as results of measurements of three masts, one with the pipe, one without the pipe and one air-circulated construction, at the same time. The information about the differences between the three construction realizations gained from the actual investigations is still meaningful.

7.2 Earlconic construction (EC-mast)

The EC-mast was built up with reinforcement plates on three sides where all plates reach up to two meters above the ground. In Figure 7.2.2 the scaled cross section of the mast and the horizontal displacement of the top of the mast is presented. The plates have azimuth values of 33°, 153° and 273°. Due to the shape, either two or all three plates are sunlit during daytime if the sky is not covered with clouds. If only two plates are under direct sunlight, the mast deforms towards the third plate as the two plates are warmed almost equally. That explains the development of the azimuth of the deformation which looks like a step function (see the second graph Figure 7.2.1). As during the night no solar radiation occurs, the deformation does not take place in direction of the third plate with an azimuth of 153°. That explains the very fluctuating direction of the displacement in the night. It appears that in the early afternoon there is almost no deformation (see the first graph in Figure 7.2.1). During that time all three plates are radiated, expand equally and cause mainly change in height. The displacement of up to 3 mm is much higher compared to the LM-mast as here the one sided radiation effects the mast much more.

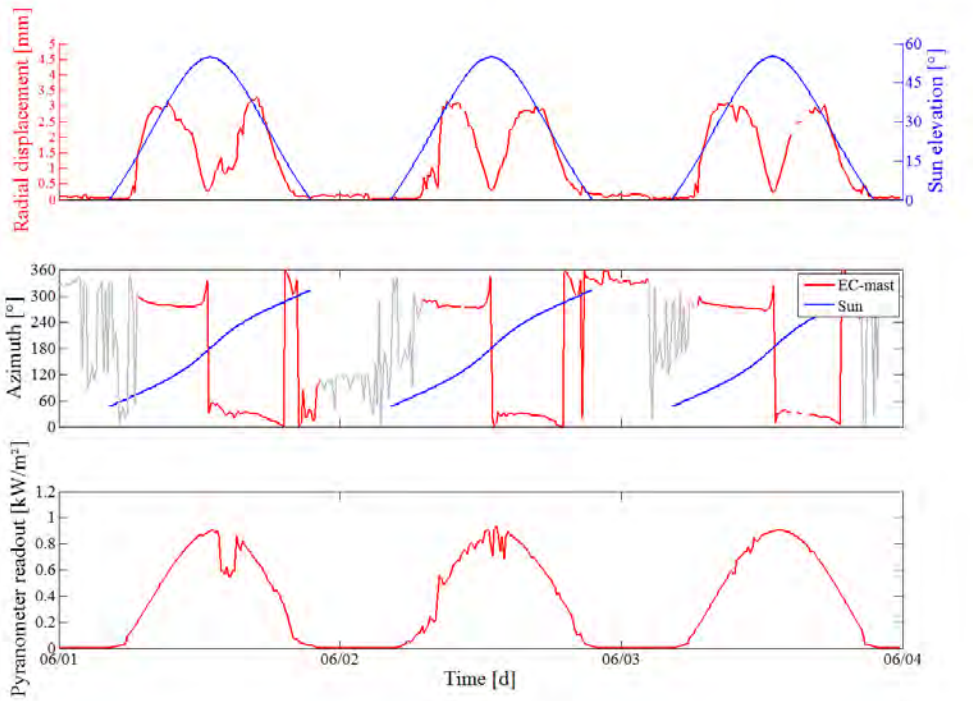

Figure 7.2.1: Time series of the sun elevation and radial displacement of the top prism of the EC-mast (top), the sun- and displacement azimuth (middle), and the solar radiation measured with the pyranometer (bottom). (Values grayed-out during periods with radial displacements <0.1 mm)

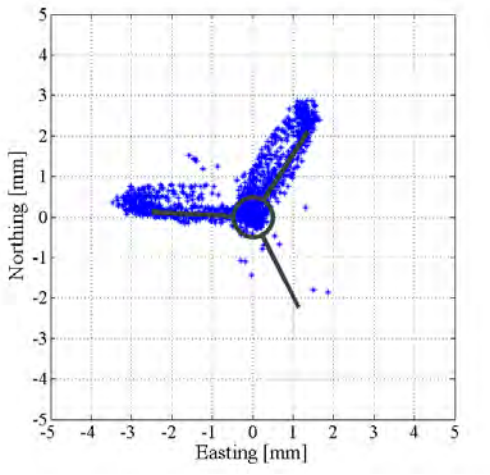

Figure 7.2.2: Horizontal deformation of the EC-mast from 06/01 till 06/23 and the scaled cross section of the mast

The steel used for that construction, "Svensk Stål SS1312", has a thermal expansion coefficient of 12 ppm/K. Between the height displacement of the EC-mast and the air temperature a linear correlation with an calculated thermal expansion coefficient of 12.8 ppm/K fit the given value of 12 ppm/K very well. The empirical standard deviation of the residuals of the mast height values is 0.15 mm. It is not as accurate as the LM-mast but still accurate enough to fit the demands of a helmert position error of <1 mm (see Figure 7.2.4).

As the mast is very massive and has no constant temperature in the entire structure, an exact thermal analysis would have needed many more sensors. Figure 7.2.3 shows the thermal expansion coefficient of 9.5 ppm/K computed with the metal temperature. In Section 5.1.2, it is shown that the sensor mounted on the sunny side of the EC-mast gives up to 10°C higher temperature values than the air temperature.

The temperature sensor was mounted on the south side of the mast and therefore measured mostly the solar radiated side of the mast, which is up to 10°C warmer than the side in the shade. The mean temperature over the whole structure can be used to find an approximation for the thermal expansion of the mast. On sunny days that value differs from the value measured with the temperature sensor.

The temperature analysis (see Section 5.1.3) show that the metal temperature in the shade is almost the same as the air temperature. It seems that the temperature in the shade dominates the whole structure.

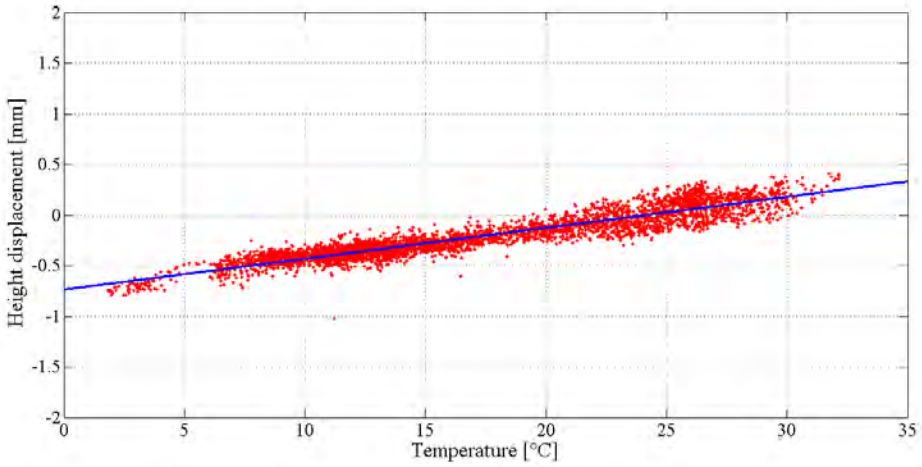

Figure 7.2.3: Relation between the metal temperature in the sun and the height displacement of the EC-mast

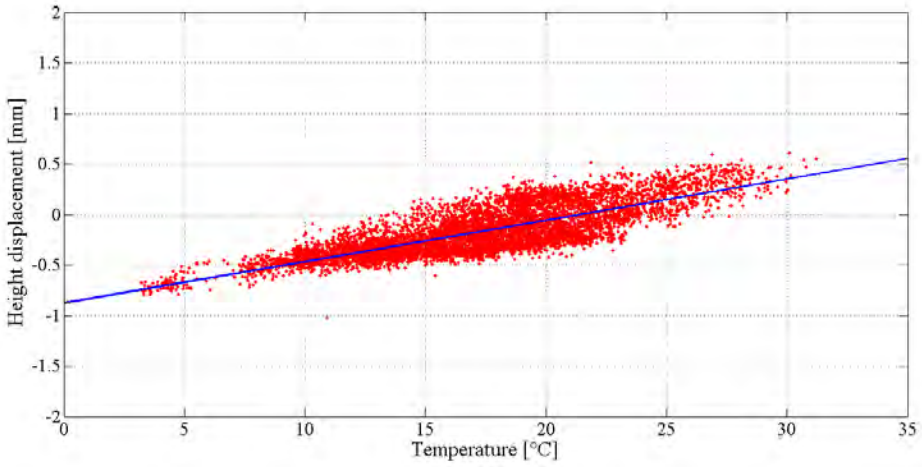

Figure 7.2.4: Relation between the air temperature and the height displacement of the EC-mast

7.3 SALSA-mast

The SALSA-mast is, compared to the EC-mast, more symmetrical. The deformations do not occur in direction of one plate but always fromward the sun.

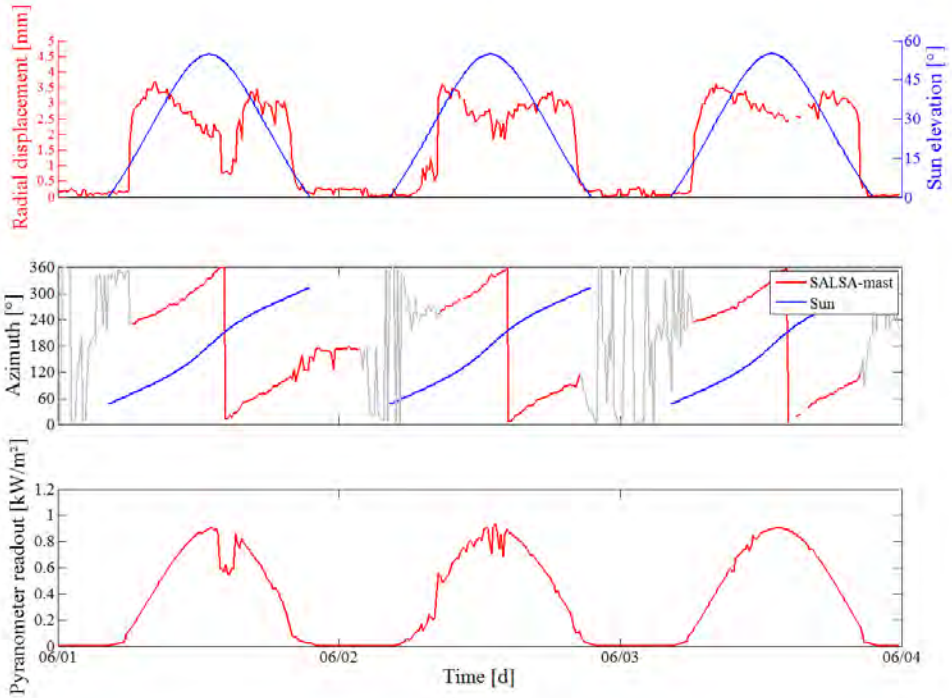

Figure 7.3.1: Time series of the sun elevation and radial displacement of the top prism of the SALSA-mast (top), the sun- and displacement azimuth (middle), and the solar radiation measured with the pyranometer (bottom). (Values grayed-out during periods with radial displacements $<0.1\,\mathrm{mm}$)

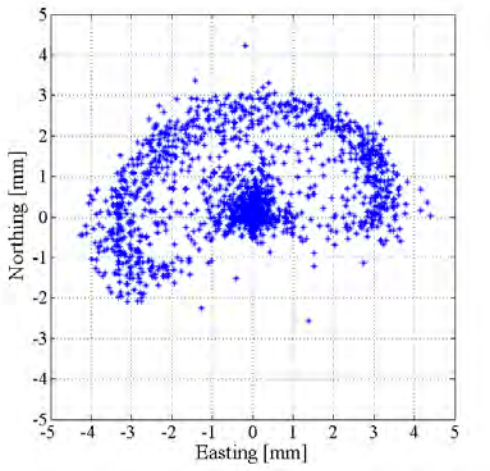

Figure 7.3.2: Horizontal deformation of the SALSA-mast from 06/01 till 06/23 with respect to the position at 2:30 on 06/01

The radial deformation reaches its maximum in the morning and evening with up to 4 mm, during midday it is a little less with up to 3 mm. The higher the air temperature is, the less is the temperature difference between the sunny and the shady side of the mast due to solar radiation. Small temperature differences result in small deformations. As the air temperature peaks at around noon, the temperature difference between the sunny and shady sides of the mast is less during that time compared to the morning and evening. In Figure 7.3.1 one can see that the peak of the radial displacement of the prism at the mast top in the evening is always less than in the morning. That can be explained by comparing air temperatures. The mean temperatures in the morning and in the evening measured during periods of the same sun elevation values differ. Statistically the air temperature during the morning hours is lower than in the evening. From the azimuth analysis it can be ascertained that the mast always moves approximately in the opposite direction to the sun as the azimuth values of the direction of the mast deformation differ during daytime by $\sim$180°. During the night, the azimuth of the deformation fluctuates very much (as discussed in Section 7.2). On the 06/01 at 14:00 there was a sudden drop in the radial deformation. The reason for that is that it was cloudy for a short while which can be read out from the pyranometer graph.

The height to temperature analysis shows that the relation is linear (see Figure 7.3.3). The empirical thermal expansion coefficient determined from the data is 12,7 ppm/K and fits well to the given value of 12 ppm/K for the "Svensk Stål SS1147-32" steel that was used.

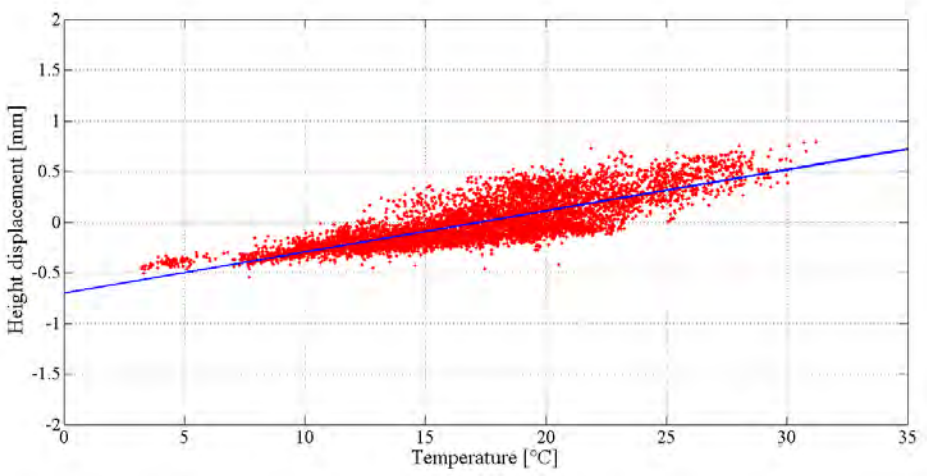

Figure 7.3.3: Relation between the air temperature in the sun and the height displacement of the SALSA-mast

7.4 SDBM-mast

The SDBM-mast analysis resulted in interesting values in some investigated relations. The displacements are very small and no relation to solar radiation, wind or temperature variation can be found. As Figure 7.4.1 shows, the maximum radial deformation is 0.4 mm. The discussion of the azimuth of the displacement direction would be very vague with such small radial displacements and was therefore not carried out. For the SDBM-mast, a type "Leica RFI" prism was used which is much smaller and less accurate than the type "Leica GMP104" prisms which were used for the other masts (see Section 4.1).

The temperature analysis resulted in very interesting graphs as shown in Figure 7.4.3. The relation between temperature and height displacement is reminiscent of a kind of S-formed function. More detailed investigations into that phenomenon would be needed to find the functional relation. At this point we can only speculate. One reason for this behavior could be the asymmetrical mounting in bedrock as the ground was uneven. The steel rods also have different lengths, and therefore expand differently due to thermal influence.

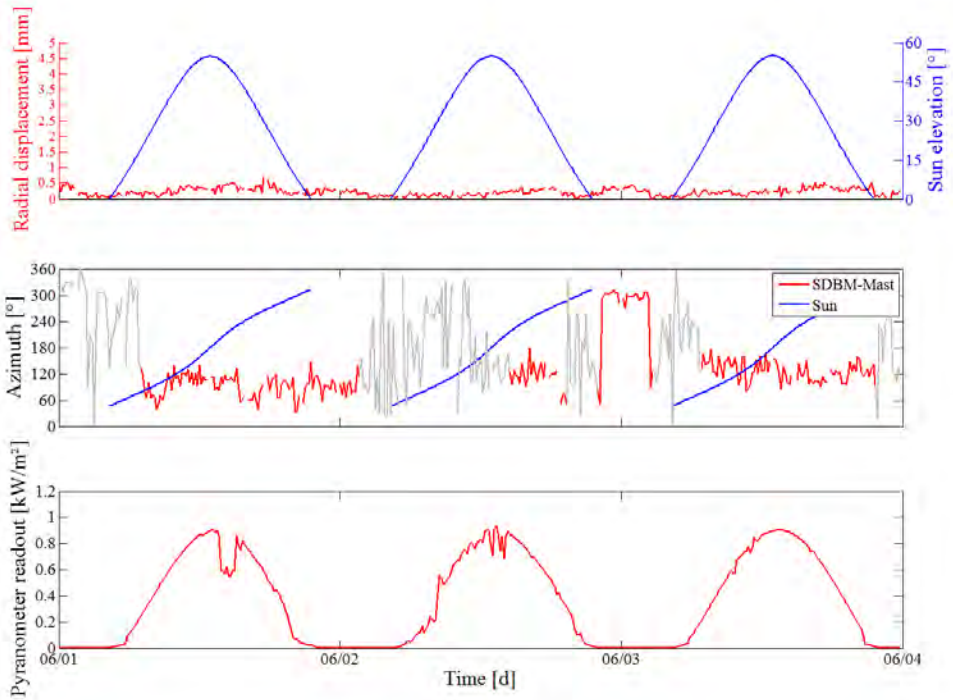

Figure 7.4.1: Time series of the sun elevation and radial displacement of the top prism of the SDBM-mast (top), the sun- and displacement azimuth (middle), and the solar radiation measured with the pyranometer (bottom). (Values grayed-out during periods with radial displacements $<0.1\,\mathrm{mm}$)

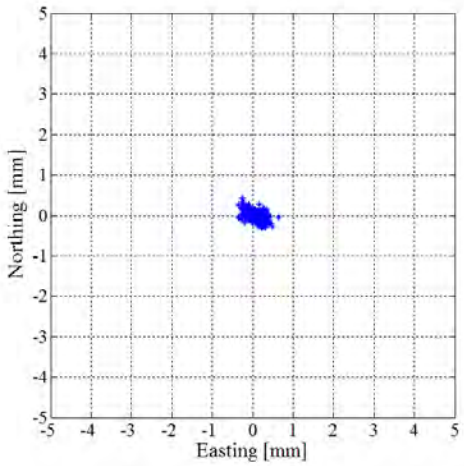

Figure 7.4.2: Horizontal deformation of the SDBM-mast

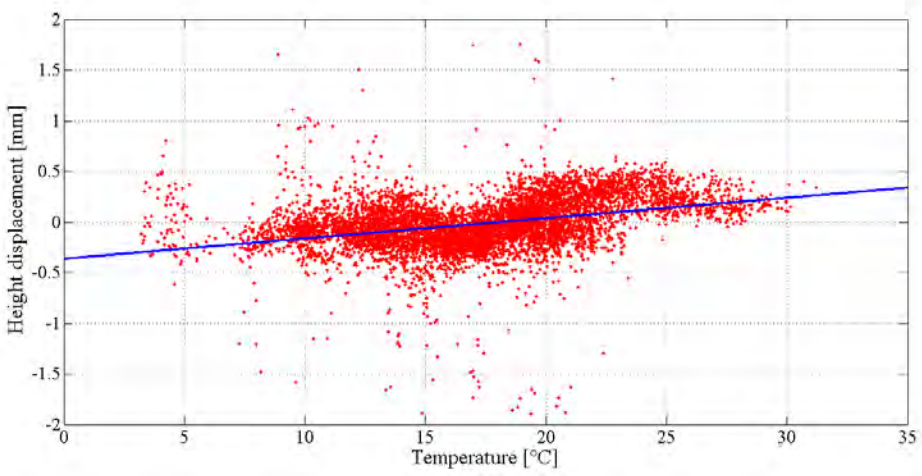

Figure 7.4.3: Relation between the air temperature in the sun and the height displacement of the SDBM-mast

7.5 Comparison of all masts

Table 7.5.1: Comparison of the maximal horizontal and vertical displacements gained from the FEM-simulation and the actual measurements. ΔT_{max}=28°C, solar radiation: E_{max}=1.05kW/m^2, measurement duration: 3 months (LM-mast results are adapted due to the different thermal expansion coefficient)

	FEM simulation			**Actual measurements**	
	Sun (ΔT=5°C)	**Temp. (ΔT=20°C)**	**Wind (30 m/s)**	**Horiz.**	**Vert.**
LM w.o. pipe	0.2 mm	0.8 mm	0.4 mm	1.1 mm	1.1 mm
LM w. pipe	0.2 mm	0.8 mm	0.3 mm	0.9 mm	1.1 mm
EC	1.0 mm	0.8 mm	1.4 mm	3.0 mm	1.0 mm
SALSA	1.2 mm	0.8 mm	1.2 mm	4.0 mm	1.0 mm
SDBM	0.1 mm	0.4 mm	<0.1 mm	1.0 mm	1.0 mm

The displacement values for the LM-mast were adapted to a thermal expansion coefficient of 12 ppm/K to be able to compare the mast with the other three. The horizontal deformation of the LM-mast is mainly due to solar radiation on the top

construction part, as the horizontal displacement is almost the same with and without the pipe which does not cover the top part. Vertically the LM-mast expands linearly with a thermal expansion coefficient of 7.5 ppm/K. In contrast to the LM-mast, the EC- and SALSA-mast have a thermal expansion coefficient of 12 ppm/K. The reason for that is, that different materials with different expansion coefficients have been used. The horizontal deformations of the EC- and SALSA-mast act on the entire structure, and not only on the top part. LM-masts with different heights have the same top construction and therefore would reach almost the same deformations as the mast with a height of 3.2 m.

Vertically the masts of different heights would expand linearly with temperature changes with an expansion coefficient of 7.5 ppm/K with the LM-mast and 12 ppm/K with the EC- and SALSA-mast. As the relation between temperature and height displacement of the SDBM-mast is not linear and not known exactly, it is not possible to make deformation predictions for different heights of the mast.

In the following the heights of the masts that theoretically would cause horizontal deformations of 1 mm will be briefly investigated. The expression 'equivalent height' will be used to describe those heights of the monuments where the theoretical values for the LM-mast with a thermal expansion coefficient of 12 ppm/K were used. The deformation shape of the LM-, EC- and SALSA-mast can be approximated by a parable.

$$dr = k_i * H^2 \qquad i \in \{1, 2, 3, 4\} \tag{7.5.1}$$

dr is the radial displacement, H is the height and k_i is a constant determined for each mast seperately by using the deformation values at the given heights of the masts.

Table 7.5.2: Height for an expected maximum horizontal deformation of 1 mm under conditions like during the above deformation measurements

LM-mast	3.37 m
EC-mast	1.84 m
SALSA-mast	1.60 m
SDBM-mast	1.25 m

The demands for determining the coordinates of the top of the masts with a Helmert position error of <1mm was reached at all masts. As the radial displacement of the truss mast even without the protective pipe is 0.8 mm at a max it would theoretically not even be necessary to correct the error of the calculated coordinates of the GNSS-antenna at the top of the mast due to environmental forces.

As described in Sections 3.2 and 3.3, the expected Helmert position error is 0.6 mm at all prisms by calculating the coordinates with distance and direction measurements, and between 0.015 mm and 0.045 mm by using forward intersection. Only ground prism two resulted in an Helmert position error higher than 0.045 mm with 0.29 mm because of the very bad geometry for forward intersection. It was not used for the project as some strange measurement results occured (see Section 5.4.1). Even if it was used

for the calculations it would only be used for controlling the orientation of the total stations. The coordinate calculation of that prism is not relevant for the project. The empirical standard deviation of the distance raw measurements for a measurement intervall of 10 minutes show values between 0.08 mm during some windless nights and up to 0.3 mm during bad weather conditions. The empirical standard deviation of the direction measurements gave values between 0.08 mgon and 2.2 mgon. The lowest values for the standard deviations of the distance and direction measurements were found in the night from 05/28 till 05/29 from 22:00 till 5:00 (clear windless night). These values are very low and seem implausible compared to the given ones from Leica with 0.6 mm+1 ppm in distance and 0.15 mgon in direction measurement. It would need more investigations to carify the reason for that very high precision. Figures 7.5.1 and 7.5.2 show the raw measurements giving the lowest values for the standard deviations. For distance the measurements from the eastern total station to ground prism three in face one resulted in the lowest standard deviation. The Hz-readings of the eastern total station to the prism at the truss mast top in face one show the lowest standard deviation in direction measurement. In Table 7.5.3 the highest and lowest empirical Helmert position error s_p of all prisms for good and bad weather conditions is presented.

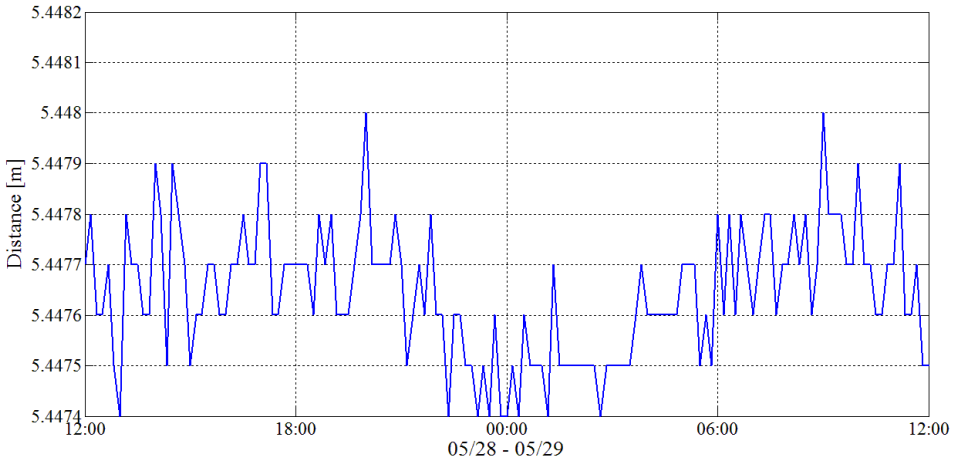

Figure 7.5.1: Time series of the distance raw measurements of the eastern total station to ground prism three in face one from 05/28 till 05/29

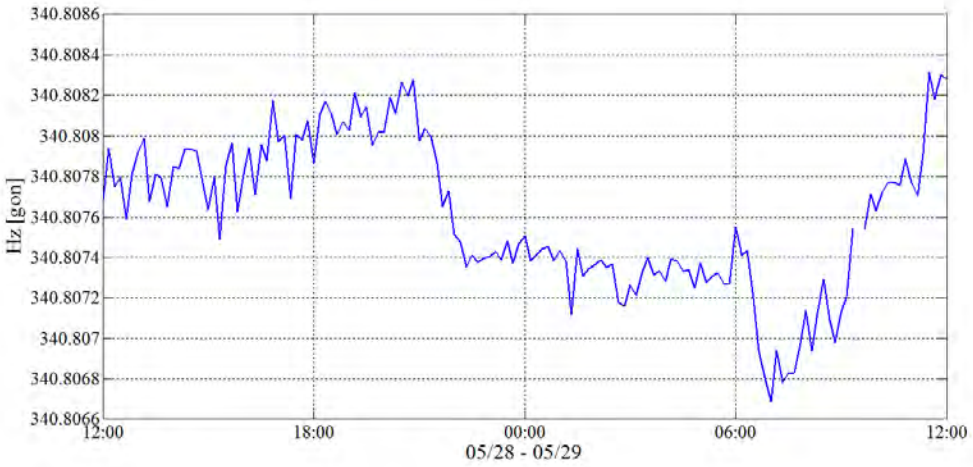

Figure 7.5.2: Time series of the Hz-raw measurements of the eastern total station to the prism at the truss mast top in face one from 05/28 till 05/29

Table 7.5.3: Comparison of the highest and lowest empirical Helmert position error of all prisms except ground prism 2.

	good weather cond.		bad weather cond.	
	$s_{p,min}$	$s_{p,max}$	$s_{p,min}$	$s_{p,max}$
forward intersection	$0.007mm$	$0.07mm$	$0.2\,mm$	$0.7\,mm$
distance and dir. measurements	$0.05\,mm$	$0.13\,mm$	$0.3\,mm$	$0.4\,mm$

Additionally, systematic errors occur. Such errors can emerge e.g. due to refraction, solar radiation of the total stations or deformation of the frames of the prisms. The error due to solar radiation at the total stations can be minimized by measuring in two faces and using the mean of both faces for the calculations of the prism coordinates.

7.6 Discussion on deformations under different conditions

The air temperature in Karesuando reached values from -36°C till +26.6°C in 2004 (see Table A.1.1) which results in temperature variations of 62.6°C at a max. Karesuando is in the very North of Sweden at a latitude of 68°. The temperature values in Säve, which is not too far from Onsala, where the actual measurements took place, showed temperature variations of 44.5°C at a max. The maximum height expansion of the mast was 0.8 mm more in the North than in the South in 2004. Above the poles the atmosphere is thinner than above the equator. As the atmosphere reduces solar radiation, the sun is more intensive in regions with a thick atmosphere than in regions

with a thin one. The radial displacement in the North would probably be higher than in the South as solar radiation is higher there.

Chapter 8

Summary and Conclusions

In this thesis four monuments for GNSS-antennas have been analyzed. One was suggested by Lantmäteriet, the Swedish mapping, cadastral and land registration authority, two are already in use in the USA and one is in use for SALSA radio telescopes at Onsala Space Observatory. The analysis was realzed in two steps. First, an FEM-modelling was done with Autodesk Robot to calculate the prospective deformations. This showed that horizontal movements of the mast top of up to 2.4 mm and vertical movements of up to 0.8 mm can be expected. The FEM modelling worked fine and gave good results for the measured deformations. Second, one sample of each mast type was set up at Onsala Space Observatory and observed almost continuously for three months using two total stations of type Leica TS30. Additionally state-of-the-art metrological equipment measured wind speed and -direction, solar radiation and temperature values at several places. Horizontal displacements of up to four millimeters and vertical displacements of up to 1 millimeters have been measured.

The mast, which Lantmäteriet suggested, deforms least with up to 0.6 mm horizontally and 0.7 mm vertically and was protected by a plastic pipe. The protective pipe is one further advantage, as it protects the mast from people climbing on it and blocks solar radiation. The construction was also investigated without the pipe but resulted in, as expected, higher deformation values. One improvement that can be made, is to mount a smaller protective pipe for surrounding the top construction of the mast that reaches directly under the antenna. It blocks the sun and can be removed easily for maintenance work.

The measurement setup works well for the demands and gives good results. Due to the fact that the total stations were mounted very close to the ground, dirt affected the instruments. Also, refraction effects are high because of the close distance to the bedrock which is much warmer than the air on sunny days and colder in the night. If a temperature-constant concrete pillar in the shade was available, the measurement accuracy would be improved and the total station would not become dirty. The mounting of the total stations and the prisms on the bedrock was realized by drilling holes and using a special glue to fix screws. The mast prisms were welded on the top of the masts. The total stations and all prisms were stable enough to fit that project.

Appendix A

Additional Information

A.1 Climate in Sweden

Sweden is located in North Europe at latitudes between 55° N and 68° N. It has a North-South distance of 1600 km (160 Swedish miles) and therefore quite different climate conditions all over the country. As shown in Table A.1.1, temperature differences of up to 63°C occur in the North during the year [SCB, 2006]. Compared to the North, the temperature changes in the South are less with up 43°C. Due to the fact that the North of Sweden is at a higher latitude than the Arctic Circle, there is no daylight during the last two weeks in December. During summer the sun does not set from late may till mid of July. The winters in Central and South Sweden are much warmer than in parts of Canada and Russia, as well as the Northern USA, although they are at the same latitude. The reason for that is the Gulf Stream. The highest air temperature in Sweden ever recorded was in Målilla at 38°C in 1947, while the coldest temperature ever recorded was −52.6°C in Vuoggatjålme in 1966. The wind speed reaches up to 30 m/s (110 km/h).

Table A.1.1: Monthly and yearly average temperature values in Sweden 2004

Month	Karesuando	Frösön	Stockholm	Säve	Lund
January	-14.6	-8.6	-2.8	-2.5	-2.2
February	-14.2	-3.7	-0.7	-0.1	1.0
March	-6.4	-0.9	1.9	2.1	3.5
April	-0.6	4.7	6.9	7.5	8.1
May	4.7	8.4	10.9	11.7	12.0
June	9.0	11.0	14.6	13.4	14.3
July	15.0	13.9	17.1	15.1	15.7
August	11.5	14.8	18.5	17.6	18.4
September	6.4	9.6	13.5	12.8	13.9
October	-0.8	3.8	7.8	8.0	9.3
November	-10.7	-1.8	1.9	3.0	4.4
December	-8.7	-1.6	1.6	3.5	3.3
Year	-0.7	4.2	7.6	7.7	8.5
Maximum	26.6	28.0	30.6	29.3	28.9
Date	6/8	10/8	8/8	7/8	6/8
Minimum	-36.0	-27.4	-13.6	-15.2	-14.1
´Date	3/1	22/1	21/1	22/1	22/1

A.2 Institutions involved in this thesis

A.2.1 SP Technical Research Institute of Sweden

SP provided most of the measuring equipment that has been used for this thesis. Also, the laser tracker Leica Absolute Tracker AT901 was provided by SP. It was used to control the adjustment computation by measuring one of the parameters, namely the length between the rotational centers of the total stations.

SP Technical Research Institute of Sweden is a leading international research institute and is the parent company of six subsidiary companies. The Swedish state is the sole shareholder.

The main areas of operations can be summarized in:

- Building and construction
- Electronics and ICT
- Energy and environment
- Fire, risk, safety and security
- Foods
- Materials technology and chemistry

- Measurement technology and calibration
- Mechanical engineering and the automotive industry
- Wood technology and wood in construction
- SP certification
- Research
- Testing

The headquarters of SP are in Borås. With a turnover of more than SEK 750 million, and a staff of about 950, SP is one of Sweden's largest research institutes. The company works together with universities and research institutes all over the world and constitutes an important link between industry and universities.

A.2.2 Lantmäteriet

Lantmäteriet gave the order to analyze the deformation behavior of the four different realizations of GNSS-antenna mast constructions. Lantmäteriet is the Swedish mapping, cadastral and land registration authority. Its mission is to manage the Swedish cadastral system and promote the rational subdivision of land, and to be responsible for the efficient provision of basic geographic and land information. It is also responsible for SWEPOS, the network of reference stations in Sweden.

Lantmäteriet provides professional services for the development and use of geographic information techniques as e.g. GNSS-positioning and maintaining the reference stations. It has a national coordination responsibility for geodata.

The main working fields are:

- Establishment and maintenance of the Swedish national, fundamental geodetic networks and for the provision of the technical infrastructure for surveying activities including satellite-based positioning and navigation.
- Promoting an appropriate and careful handling of place names and formally approving place names.
- Carrying out development activities within Lantmäteriet's fields of activity and doing geodetic research.

A.2.3 Onsala Space Observatory

At Onsala Space Observatory all measurements have taken place from mid-May till mid-August.

Three alternative mast constructions have been built and equipment, as e.g. a laptop for continuous outdoor usage, a digital multimeter, many cables, and so on, was provided. Onsala Space Observatory is located 45 km south of Göteborg is part

of Chalmers University of Technology and uses two telescopes of 20 m and 25 m in diameter.

Projects, in which Onsala Space Observatory is involved, are:

- APEX: Radio telescope in Chile for sub-millimeter waves.
- Odin: Satellite for studies of, e.g., the Earth's atmosphere and molecular clouds in the Milky Way.
- ALMA, e-VLBI, Herschel, LOFAR, SKA: Developing and using new radio astronomical facilities.
- Space geodesy: Radio telescopes (VLBI), satellites (GPS) and gravimeters are used to measure Earth's rotation, movements in Earth's crust, and water vapor in the atmosphere.
- Receiver development: Laboratories for development of sensitive radio receivers.
- The 20 and 25 m telescopes in Onsala are used for
  - studies of the birth and death of stars, and of molecules in the Milky Way and other galaxies.
  - VLBI: Telescopes in different countries are linked together for better resolution ("sharper images").

A.3 SWEPOS

SWEPOS is the network of reference stations in Sweden Gunnar Hedling et al. [2009].

It consists of 188 permanent reference stations where, depending on the foundation, two different types of stations are in use. Class A stations are mounted on pillars or masts, which are analyzed in this thesis, and Class B stations are usually mounted on the roof of buildings.

The idea behind this thesis is to investigate in masts which should be used for new reference stations for the SWEPOS system.

The goals of SWEPOS are:

- Supplying GNSS-data for navigation, positioning, science and education.
- Act as the basis for the realisation of the National Reference System: SWEREF 99.
- Checking the integrity of the GNSS systems.

Bibliography

K. Fischer. Sternpyranometer, 2005.

Gunnar Hedling, Peter Wiklund, Anna Lööf, Martin Lidberg, and Bo Jonsson. New Developments in the SWEPOS Network. 2009.

Heribert Kahmen. *Angewandte Geodäsie: Vermessungskunde*. Walter de Gruyter, 2006. ISBN 3110184648.

Leica. Leica Geosystems Reflectors, 2000.

Leica. Leica Original Accessories. Technical report, Leica Geosystems AG, Heerbrugg, Switzerland, 2010.

Gerhard Navratil. *Ausgleichungsrechnung I.* 2008a.

Gerhard Navratil. *Ausgleichungsrechnung II.* 2008b.

Wolfgang Niemeier. *Ausgleichungsrechnung: Statistische Auswertemethoden, 2. Auflage*. Walter de Gruyter, 2008. ISBN 3110190559.

SCB. Sweden in Figures. 2006.

Andrew Semenchuk. MDOT CORS Earlconic Specifications, 2007.

UNAVCO. Shallow Braced (non-drilled) Monument, 2010.

J. Uren and William Frank Price. *Surveying for engineers*. Palgrave Macmillan, 4 edition, 2006. ISBN 1403920540, 9781403920546.

Hans-Martin Zogg, Werner Lienhart, and Daniel Nindl. Leica TS30 White Paper. 2009.